
Structural Investigations of Membranes of Interest in Biology by Neutron Reflectometry

C.F.Majkrzak, N.F.Berk, S.Krueger, and U.A.Perez-Salas

National Institute of Standards and Technology, Gaithersburg, MD 20899

1 Introduction

Membranes are an essential part of every living cell. Determining the nanometer scale structure of these partitions is of interest for the understanding of important cellular processes on a molecular level, including, for example, transport mechanisms into and out of the cell interior and the functioning of protein sensors embedded in the membrane [1].

In "real" space, probes such as atomic force and electron microscopies, at present, can provide localized images of a material *surface* with nanometer scale resolution. However, *scattering* techniques employing neutrons and x rays have proven to be especially well-suited for "viewing", in comparable detail, the distribution of matter *beneath* the surface. The reasons for this subsurface sensitivity are manifold, but principally are a consequence of the wave nature of the radiation, the relative strengths of interaction (between photon and atomic electrons or between neutron and nucleus), and the ability to accurately measure and analyze the diffraction pattern that the material density distribution of the film gives rise to.

The sensitivity of diffraction as a probe of membrane structure is considerably enhanced if a homogeneous specimen of the film can be constrained to lie on a flat surface (either a solid or liquid substrate). A membrane so confined is, effectively, a quasi two- dimensional scattering object. Treating the neutron as a plane wave, having a wavevector k proportional to its momentum, the coherent (in phase), elastic (no energy transfer) reflection of that neutron from a flat film can be then separated into two distinct types, specular and nonspecular. Specular scattering refers to the condition in which the glancing angle θ between the reflected neutron wavevector and the surface is equal to that of the incident wave. In this case the momentum transfer is exactly perpendicular to the surface. Analysis of the specular reflectivity reveals the depth profile of the film's density along the surface normal. If there are no variations in the composition or material density within the plane of the

film, then *only* specular scattering can occur. In a case where in-plane fluctuations of the density are present, the specular component of the reflected intensity is caused by a film density that is averaged, at a given depth, over the in-plane area for which the neutron plane wavefront is coherent (typically of the order of microns). In addition, however, in-plane fluctuations produce nonspecular scattering wherein the momentum transfer has a component parallel to the surface. Nonspecular scattering data thus contains information about in-plane structure. Nonspecular reflectometry has great potential for the study of biofilms, for example, in determining the sizes and distribution of various entities, such as cholesterol "rafts", within the plane of a membrane. However, research in this area is not yet as developed as that involving specular reflectometry. The reasons for this involve a number of technical difficulties, including the preparation of specimens of sufficient size and homogeneity and the theoretical interpretation of the nonspecular scattering, particularly at wavevector transfers where the Born approximation (discussed below) is not valid. The present Chapter is concerned primarily with specular reflection. The interested reader is referred elsewhere for discussions of nonspecular scattering, e.g. ref. [2, 3].

The resolution of a material distribution in real space deduced from diffraction data is, ultimately, inversely proportional to the range in wavevector transfer Q over which the reflected intensity is measured. The wavevector transfer for the reflected beam is $k_f - k_i = -2k \sin(\theta) = -4\pi \sin(\theta)/\lambda = -2k_{0z}$, where k_{0z} is the component of the incident wavevector normal to the film. We will always define $Q = 2k_{0z}$, so that the reflected wavevector transfer is $-Q$. For instance, the spatial resolution in the compositional depth profile obtained from analysis of the specular reflectivity (defined as the reflected intensity divided by the incident intensity) measured out to a wavevector transfer of 0.7 \AA^{-1} corresponds to a spatial resolution of the order of 0.5 nm. Given the strength of available neutron sources, sample areas of several square millimeters or more are therefore necessary in practice to obtain sufficiently accurate data. Reflectivity experiments (*i.e.*, "reflectometry") conducted over a range of wavevector transfers similar to that just given are to be distinguished from diffraction studies performed at higher wavevector transfers corresponding to interatomic scale resolution.

The purpose of this contribution is to provide an overview of the experimental and theoretical methods now employed in the study of membrane structures by specular neutron reflectometry. Nonetheless, a reasonable amount of detail is included here so that the researcher new to the technique can better judge what structural information is obtainable from reflectometry and can assess what actually is required to prepare a suitable specimen, perform measurements, and subsequently analyze the data. Reviews of current research in which neutron reflectometry has been applied to the study of biological or biomimetic membrane structures, including systems with embedded proteins and peptides, are given in other contributions of this book by Lu, Gutberlet et al. and elsewhere [4]. However, a representative example

of a neutron reflectometry study of a lipid bilayer membrane into which the peptide melittin has been introduced is included here, to further illustrate the technique.

2 Theory

The theory of neutron reflectivity and diffraction is well-established [5, 6, 7, 8, 9, 10], although there have been relatively recent developments in methods for phase determination and inversion (see, for example, the review [11] and references therein). This Section summarizes key features of the theory pertinent to the study of thin films and membranes.

2.1 The Exact ("Dynamical") Solution

The specular reflectivity from a flat surface or film effectively reduces to a one-dimensional wave mechanics problem (see Merzbacher [13], for example)

$$-\frac{\partial^2 \psi(z)}{\partial z^2} + 4\pi\rho(z)\psi(z) = k_{0z}^2 \psi(z), \quad (1)$$

where k_{0z} is the wavevector of the neutron in vacuum and $\rho(z)$ is the the scattering length density (SLD) "profile," which describes the neutron interaction with the film and its surrounding media everywhere along the z -axis, normal to the film surface. For neutrons with wavelengths of the order of several ångströms, the SLD at any "point" is the compositionally weighted average of the coherent neutron scattering lengths in a volume element having linear dimensions on the order of the neutron wavelength, divided by the volume of the element. Scattering length densities thus have dimensions of inverse area. Scattering lengths are the fundamental measure of the neutron–nucleus interaction and vary from one isotope to another in an essentially random but fixed manner. Coherent, in this context, refers to the component of the interaction that enables neutrons scattered by nuclei at different points in the film to interfere, much as ripples on a pond. It is such interference which makes the scattering dependent on spatial structure.

We have assumed the ideal situation for specular scattering where the SLD varies only along the surface normal. In general the SLD $\rho(x, y, z)$ can vary in all three directions in the film, so that the true reflection problem is inherently three-dimensional. Thus, the SLD $\rho(z)$ appearing in eq. 1 is defined as

$$\rho(z) = \lim_{S \rightarrow \infty} \frac{1}{S} \iint_S \rho(x, y, z) \, dS \equiv \langle \rho(x, y, z) \rangle_{xy}, \quad (2)$$

where S denotes the surface area of the film. In-plane variations of the SLD give rise to non-specular scattering. In the most extreme case, the specular reflection caused by $\rho(z)$ and the non-specular reflection caused by $\Delta\rho(x, y, z)$

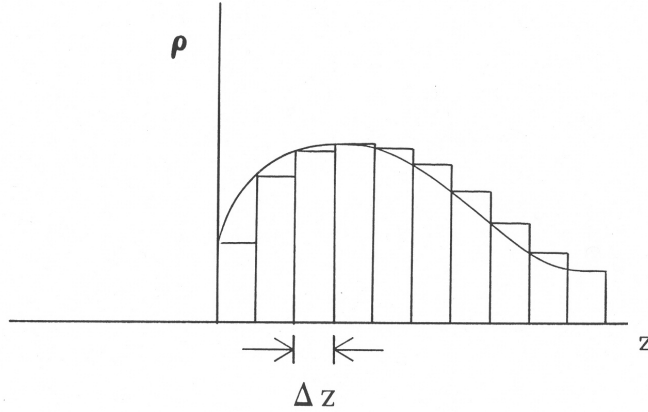


Fig. 1. Scattering length density depth profile, along the surface normal, of arbitrary shape represented by rectangular bins or slices over each of which the density is taken to be constant.

interfere with one another, so that the resultant reflectivity can not be expressed as two distinct contributions. However, in many cases of interest, either the non-specular component is negligible or the two contributions are separable. When lateral variations of the SLD are random, the measured reflectivity represents a "thermodynamic" average of the reflectivity over a suitable ensemble of such configurations. For cases where $\rho(x, y, z)$ is "self-averaging," *i.e.*, where $\langle \rho(x, y, z) \rangle_{xy} = \langle \rho(x, y, z) \rangle_{\text{therm}}$, it can be shown that the specular reflection determined by $\rho(z)$ and the non-specular reflection induced by the residual $\Delta\rho(x, y, z)$ are decoupled from one another [14]. Even then, however, we need to know how to separate them. The specular reflectivity is defined as the ratio of the specularly reflected intensity to the incident intensity; the non-specular intensity affects both. When the instrument is configured to collect the specular signal (*i.e.*, on the *specular ridge*), some fraction of the non-specular intensity is also counted and, therefore, must be subtracted. At the same time, non-specular intensity in other directions diminishes incident intensity which would otherwise cause specular reflection.

For both computational and analytic purposes, an SLD profile $\rho(z)$ of any shape can be accurately represented, for measurements up to a finite maximum $Q = Q_{\text{max}}$, by a piecewise continuous subdivision, $\rho_{\text{pwc}}(z)$, into a sufficient number of rectangular slices, or "bins" of widths $\Delta z \ll \pi/Q_{\text{max}}$, where the SLD within each slice is taken to be constant, as depicted schematically in Fig. 1. The fundamental quantity describing the specular reflection of the neutron by the membrane is the spectrum (as a function of Q) of the reflection amplitude r , a complex number, $r = |r|e^{i\phi}$ of modulus $|r|$ and a phase ϕ .

Similarly, the transmitted wave is characterized by a transmission amplitude t , but it turns out that all of the relevant information is contained in the spectrum of r . To set up equations which describe the relationship between r , t , and ρ , we first make the piecewise continuous rendering of $\rho(z)$ explicit with

$$\rho_{\text{pwc}}(z) = \begin{cases} \rho_j & \text{if } (j-1)\Delta z \leq z < j\Delta z \\ 0 & \text{otherwise} \end{cases}, \quad (3)$$

where $j = 1, \dots, N$. Thus $\rho_{\text{pwc}}(z)$ is a "histogram" of N bins of uniform width $\Delta z = L/N$, where $\rho_{\text{pwc}}(z) = \rho_j$ in the j -th bin. Next, we partition the z -axis (along the film normal) into three contiguous regions: region I, the "fronting," where $z < 0$; region II, the "film of interest," where $0 \leq z \leq L$; and region III, the "backing," where $z > L$. The fronting is defined as the region containing the incident and reflected beams, while the backing is the region of the transmitted beam, regardless of how the film is mechanically supported. In region I, $\rho(z) = \rho^{\text{I}}$, and in region III, $\rho(z) = \rho^{\text{III}}$, where ρ^{I} and ρ^{III} are known constants (typically, the SLD values for air or vacuum, silicon, sapphire, and mixtures of water and heavy water, as appropriate to the experiment). With each of the regions of constant SLD, *viz.*, I and III and in the slabs comprising ρ_{pwc} in II, we can associate a wavevector component along the z -axis

$$k_z^{\text{I,II,III}} = k_{0z} \sqrt{1 - 4\pi\rho^{\text{I,II,III}}/k_{0z}^2} \equiv n_z^{\text{I,II,III}} k_{0z}. \quad (4)$$

(From now on we will suppress the " z " subscript on k .) Note that in region II, where $\rho = \rho_{\text{pwc}}$ has values ρ_j , k_z^{II} has the corresponding values k_j^{II} . In regions I and III, the physical solutions of eq. 1 have the simple plane wave forms [15]

$$\psi^{\text{I,III}}(z) = \begin{cases} e^{ik^{\text{I}}z} + re^{-ik^{\text{I}}z} & \text{for } z < 0, \\ te^{ik^{\text{III}}z} & \text{for } z > L, \end{cases}. \quad (5)$$

These solutions (and their derivatives) are "transferred" across region II by the matrix equation [15, 11],

$$\begin{pmatrix} t \\ in^{\text{III}}t \end{pmatrix} e^{ik^{\text{III}}L} = M \begin{pmatrix} 1+r \\ in^{\text{I}}(1-r) \end{pmatrix} \quad (6)$$

where the *transfer matrix* $M = \begin{pmatrix} A & B \\ C & D \end{pmatrix}$ is a 2×2 real valued matrix having unit determinant, $AD - BC = 1$. For ρ_{pwc} , this is the matrix product

$$M = M_N M_{N-1} \cdots M_j \cdots M_2 M_1, \quad (7)$$

where M_j is the transfer matrix for the j -th bin,

$$M_j = \begin{pmatrix} \cos(k_j^{\text{II}} \Delta z) & \sin(k_j^{\text{II}} \Delta z)/n_j^{\text{II}} \\ -n_j^{\text{II}} \sin(k_j^{\text{II}} \Delta z) & \cos(k_j^{\text{II}} \Delta z) \end{pmatrix} \quad (8)$$

In general eq. 7 can represent any useful decomposition of $\rho(z)$ into N contiguous, non-overlapping segments.

Equation 6 stands for two simultaneous linear equations, which are straightforwardly solved for r and t as a function of the matrix elements A, B, C , and D as functions of k_{0z} . For the case of a "free" film, *i.e.*, a film in contact with vacuum fronting and backing, the result for the reflection amplitude is

$$r = \frac{B + C + i(D - A)}{B - C + i(D + A)} = \frac{B^2 + D^2 - A^2 - C^2 - 2i(AB + CD)}{A^2 + B^2 + C^2 + D^2 + 2}, \quad (9)$$

while the reflectivity, $|r|^2 = r^* r$, is most simply represented by

$$2 \frac{1 + |r|^2}{1 - |r|^2} = A^2 + B^2 + C^2 + D^2. \quad (10)$$

While it is straightforward to compute the reflectivity for a given model SLD profile, the so-called "direct problem", deducing ρ from reflectivity data, the "inverse problem", is much more problematic and inherently ambiguous because of the "lost" phase angle ϕ . Indeed, we see from eq. 9 and eq. 10 that full knowledge of r needs three combinations of A, B, C , and D , *viz.*, $A^2 + C^2$, $B^2 + D^2$, and $AB + CD$ (because $AD - BC = 1$, these are not completely independent); while knowledge of $|r|^2$ implies only the sum of squares combination, $A^2 + B^2 + C^2 + D^2$. In practice, the determination of an SLD profile from reflectivity data employs fitting schemes based on either model-dependent or model-independent methods (see ref. [17, 18], for example). Figure 2 shows SLD profiles for a pair of model thin film structures, having thicknesses and SLD values typical of those of interest to us here (Fig. 2a), and the corresponding specular neutron reflectivities (Fig. 2b), which are nearly identical and thus demonstrate the importance of phase information—or its absence. Even though it might not be possible to deduce from the reflectivity alone which of two or more SLD profiles is the veridical one, *i.e.*, the one that actually produced the data, it can be concluded whether or not a given model SLD profile is at least consistent with the measured reflectivity. Furthermore, a priori knowledge of the SLD in part of the film or the adjacent substrate can be used to recover, in effect, some of the phase information: this can also be accomplished by controlled manipulation of the SLD in certain sections of the film, *i.e.*, by exchanging hydrogen for deuterium [19]. Such partial phase information can significantly reduce the number of acceptable solutions.

Methods have been developed to recover phase information through the use of various reference structures—either adjacent films or surrounding media [20, 21, 22, 23, 24, 25]. For some of these, the reflection amplitude for the unknown part of the film can be obtained "locally" (*i.e.*, independently at

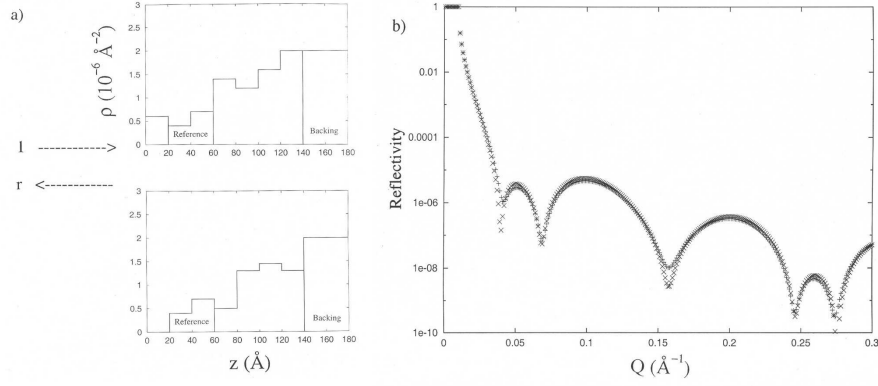


Fig. 2. (a) Model SLD (neutron) profiles similar to two of the profiles considered for x-ray reflection (Fig. 3 of Ref. [44]). Both profiles share a common "reference" or known segment between $z = 20 \text{ \AA}$ and $z = 60 \text{ \AA}$. (b) Corresponding neutron reflectivity curves calculated for the two composite SLD profiles in (a). The two curves are practically indistinguishable from one another (after Fig. 10 of Ref. [16]).

any k) and exactly [22, 24]. It has been shown, that the reflection amplitude and the SLD profile are in one-to-one correspondence for a large class of film potentials. This means that the given profile produces a unique spectrum of r and that a given r , if known for all Q , produces a unique SLD profile, when using the appropriate mathematical tools to retrieve it [26]. Figure 3 shows the real part of r (multiplied by Q^2) for each of the two model SLD profiles of Fig. 2a: in stark contrast to the two corresponding reflectivity curves of Fig. 2b, there is a marked, clearly distinguishable difference. An actual example which demonstrates the phase inversion technique is given in Section 5. In practice, the solution of the inverse problem is limited by the finite range of Q over which it is possible to measure the reflectivity, but ambiguities introduced by data truncation are systematic and, to a limited extent, treatable [27, 12].

The reflection amplitude has a number of useful theoretical representations. If we know the solution ψ of eq. 1 in region II, then an alternative, and quite general, expression for the free film r can also be derived [28] using the wave equation in eq. 1,

$$r = \frac{4\pi}{2ik_{0z}} \int_{-\infty}^{\infty} \psi(z) \rho^{\text{II}}(z) e^{ik_{0z}z} dz. \quad (11)$$

Because ψ depends on r , eq. 11 actually represents an implicit equation for r , but it does provide a useful starting point for formal analysis and for some practical approximation schemes.

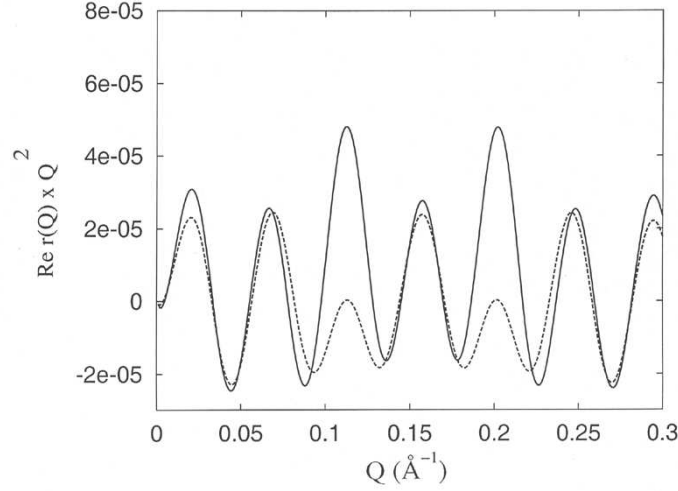


Fig. 3. $Q^2 \text{Re} r(Q)$ for the (reversed) film structures of Fig. 2a (not including the backing but incorporating the known or reference sections of the films). These $\text{Re} r(Q)$ correspond to what would be retrieved, for example, by phase-sensitive reflectivity experiments (for each of the two SLD profiles) in which the backing SLD was varied according to the methods discussed in the text. In contrast to the situation illustrated in Fig. 2b, these curves are markedly different over a wide range of Q . (After Fig. 9 of ref. [16].)

2.2 The Born Approximation

In general, as seen from eq. 11, the weaker the potential and the higher the wavevector transfer, the smaller the reflectivity becomes. For reflectivities of the order of a few percent or less, the neutron wave function within the scattering medium is not significantly distorted from its free space, plane wave form. In this case, $\psi(z)$ in eq. 11 can be approximated by the incident wave function, leading to the Born approximation (BA) or so-called "kinematic" result,

$$r^{\text{BA}}(Q) = \frac{4\pi}{iQ} \int_{-\infty}^{\infty} \rho^{\text{II}}(z) e^{iQz} dz, \quad (12)$$

Thus, $Qr^{\text{BA}}(Q)$ and $\rho^{\text{II}}(z)$ are related by Fourier transformation. The factor of Q^{-1} multiplying the integral in eq. 12 does not result from the BA; it is the same factor appearing in eq. 11, the general expression, and is inherent in the effective one-dimensionality of the specular reflection problem (*i.e.*, the infinite-slab geometry of the 3-D problem). The essential difference is that the exact $\psi(z, Q)$ approaches zero as Q goes to zero, unlike its plane wave approximation, thus keeping $r(Q)$ finite at $Q = 0$ in eq. 11. Of course, it is

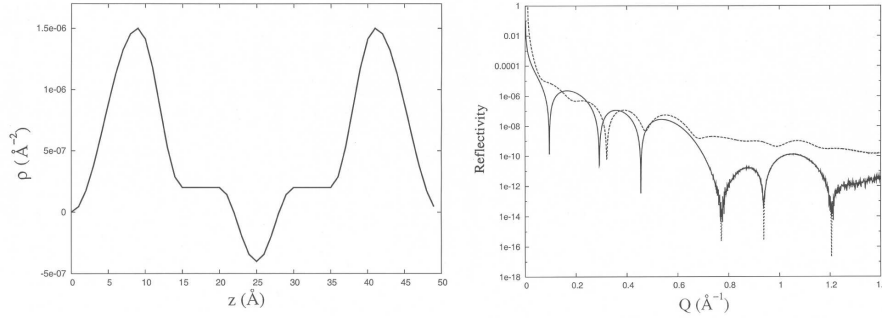


Fig. 4. Model SLD profile for a lipid bilayer as discussed in the text (left). Specular reflectivity for the SLD profile calculated according to the exact theory as well as in the Born approximation, assuming the bilayer to be free standing (right). Also plotted is the reflectivity calculated according to the exact theory for the same bilayer film but on a semi-infinite substrate of Si. The reflectivities according to the exact theory and the BA are virtually indistinguishable on a logarithmic scale for the free standing films, except in the neighborhood of the origin. Only the reflectivity for the film on the substrate has a region of total external reflection (long-dashed curve).

to be expected that the BA will fail as $Q \rightarrow 0$, since, as $|r(Q)| \rightarrow 1$ at the origin, $\psi(z, Q)$ becomes poorly approximated in region II by the "undistorted" incident wave. Figure 4 shows a model SLD profile for a lipid bilayer similar to that deduced in a neutron reflectivity study of DOPC multilayers by Wiener and White [29]. In Fig. 4 the specular neutron reflectivity $|r|^2$ for the SLD profile is plotted as a function of Q , calculated using the exact theory and in the Born approximation for a freely standing single bilayer surrounded by vacuum. Also shown is the reflectivity for the same bilayer on a substrate (thick enough that it is effectively semi-infinite) as predicted by the exact theory. In the latter case the Born approximation would fail not only at the origin, but also in the neighborhood of the critical angle for total external or mirror reflection (below which the reflectivity is unity).

2.3 Multilayers

In certain cases it is advantageous to reflect from a repeating or multilayered assembly of membrane films instead of a single membrane unit. Since the reflection from such structures tends to be concentrated at higher Q -values than for single-layer thin films, the Born approximation can be particularly valuable in analyzing reflection from them. For a periodic multilayer structure (assuming ideally flat, parallel layers of uniform density and thickness), the reflection amplitude in the BA is given by (ref. [28], for example)

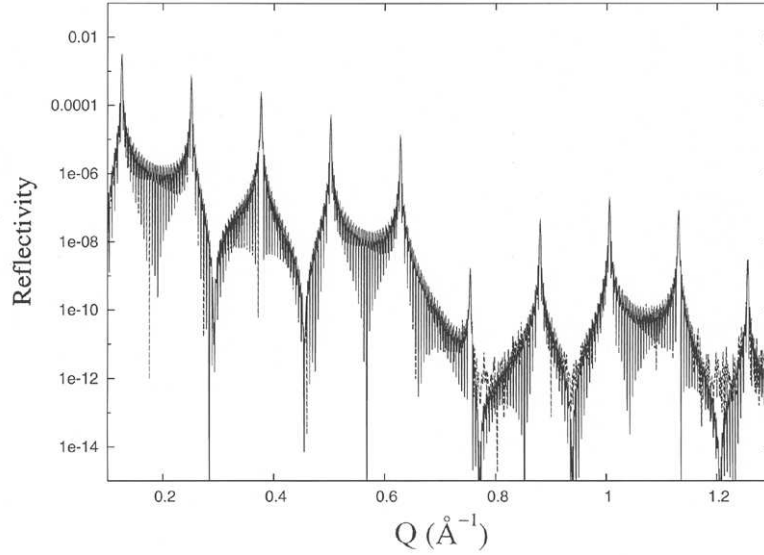


Fig. 5. Comparison of the reflectivities, calculated according to the exact and kinematic formulas, for $M = 50$ bilayers having the SLD profile of Fig. 4 (assuming no substrate).

$$r_{\text{ML}}^{\text{BA}}(Q) = \frac{4\pi}{iQ} \left[\frac{\sin(MQD/2)}{\sin(QD/2)} \right] e^{i(M-1)DQ/2} \int_0^D \rho(z) e^{iQz} dz, \quad (13)$$

for M repeats of a unit film (*e.g.*, the bilayer) of thickness D . The integral over $\rho(z)$ is limited to the unit film. The effect of the M repeats appears only in the prefactor, where (using L'Hospital's rule) the ratio of sine functions in brackets acts as a concentrator of reflection about the *Nyquist lattice* points, $Q = Q_m$, as M increases, where $Q_m = 2\pi m/D$ for integer m . Thus, for M large (but not so large as to invalidate the BA), $r_{\text{ML}}^{\text{BA}}(Q)$ is strongly peaked on the Nyquist points, in the manner of Bragg peaks in crystallography. Fig. 5 compares the reflectivities, calculated with the exact and kinematic formulas, for $M = 50$ bilayers having the SLD profile of Fig. 4 (and assuming no substrate). Note how the reflected intensity of the multilayer is localized about the Nyquist lattice, in contrast to being more uniformly distributed over the entire Q -range, as evident in Fig. 4. Clearly the kinematic theory can give a good account of multilayer reflection.

Now the SLD profile of Fig. 4 is centrosymmetric along the z -axis and can, consequently, be represented by a Fourier cosine series [30]

$$\rho(z) = A_0 + 2 \sum_{m=1}^{\infty} A_m \cos(Q_m z) \quad (14)$$

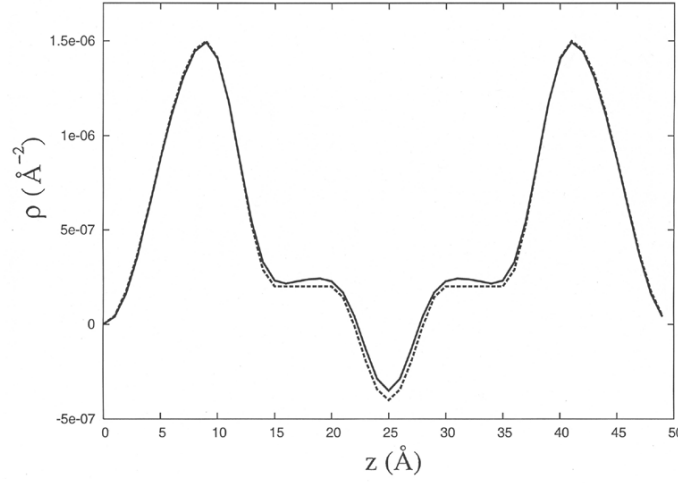


Fig. 6. SLD profile of Fig. 4 (dashed curve) compared to that obtained by the Fourier series analysis of the reflectivity curve (exact result) in Fig. 5 described in the text.

where the A_m are real numbers.

From the reflectivity curve plotted in Fig. 5 (corresponding to the bilayer of Fig. 4, with $M = 50$), the peaks up to the 10-th order, inclusive, were used to determine the Fourier series of eq. 14, truncated at $m = 10$. The resulting $\rho(z)$ is plotted in Fig. 6, along with the original SLD profile of Fig. 4 for comparison. The agreement displayed in Fig. 6 is qualitatively good. But even 10 perfectly "measured" orders do not provide all the detail in the veridical $\rho(z)$.

2.4 Scale of Spatial Resolution

In assessing the value of SLD profiles inferred from reflection measurements, we must know how much spatial detail is meaningful to expect from the analysis; i.e., we can ask, what is the scale of spatial resolution – let us quantify this as a length l – of the resulting $\rho(z)$?

Let us say that we have perfect knowledge of the reflection amplitude $r(Q)$ up to a maximum value of $Q = Q_{\max}$. (The experimental factors determining Q_{\max} will be discussed in a later section.) The dominant factor limiting the spatial resolution ℓ of $\rho(z)$ inferred from this knowledge is the value of Q_{\max} , according to $\ell = \pi/Q_{\max}$ [11, 12]. For our purposes, this holds that the number of spatial degrees of freedom N in $\rho(z)$ for a film of thickness L , when $r(Q)$ is known for $|Q| \leq Q_{\max}$ is given by (the integer part of) $N = Q_{\max}L/\pi$, referred to variously as the Nyquist or the Slepian number. Associating the

corresponding scale of spatial resolution with $\ell = L/N$, one has $\ell = \pi/Q_{\max}$ directly. In addition [12], ℓ also emerges explicitly from wavelet representations of $\rho(z)$, where ℓ is identified with the scale length of its most rapidly varying "detail," and N is the number of wavelets needed to fully describe $\rho(z)$ on this length scale. Indeed [11], as a special case, if we model $\rho(z)$ by N bins of uniform SLD and equal widths ℓ , as in $\rho_{\text{pwc}}(z)$ of eq. 3, then $r_{\text{BA}}(Q)$ in eq. 12 is exactly invertible for $\rho_{\text{pwc}}(z)$ over the Q -range, $|Q| \leq Q_{\max}$, where $Q_{\max} = \pi/\ell$.

Now in general [12], let $r(Q)$ be perfectly known for $|Q| \leq Q_{\max}$, and call this conditional knowledge the function $r(Q|Q_{\max})$. Then the inversion of $r(Q|Q_{\max})$ by a fixed procedure—namely the one we would use for $Q_{\max} = \infty$, but setting $r(Q|Q_{\max}) = 0$ for $Q > Q_{\max}$ —determines a distorted or "smeared" version of the veridical $\rho(z)$, say $\rho(z|Q_{\max})$, which effectively parameterizes $\rho(z)$ on the spatial scale ℓ . The maximum Q of the measurement thus inherently limits the spatial resolution of $\rho(z)$ that can be reliably determined; the larger the value of Q_{\max} , the smaller the scale ℓ of detail we can know reliably.

What if our knowledge is limited to the reflectivity $|r(Q|Q_{\max})|^2$? If we consider the Born approximation, eq. 12, as an adequate basis for analysis, then we may appeal to the well-known result that the Fourier transform of $Q^2|r^{\text{BA}}(Q)|^2$ directly determines the auto-correlation function

$$\gamma(z) = \int_{-\infty}^{\infty} \rho(z - z')\rho(z') dz', \quad (15)$$

which describes the smearing of $\rho(z)$ by itself. This implies that for given Q_{\max} , if $\rho(z|Q_{\max})$ is resolved to scale ℓ , then $\gamma(z|Q_{\max})$ is resolved to scale 2ℓ . More carefully, if $\rho(z)$ is supported on an interval of length L , then $\gamma(z)$ has support of length $2L$. Thus applying the *same number* of spatial degrees of freedom to $\rho(z|Q_{\max})$ and to $\gamma(z|Q_{\max})$ leads to a scale of resolution $2\ell = 2\pi/Q_{\max}$ for the latter. The loss of phase information thus leads to a loss of spatial resolution for finite Q_{\max} .

3 Basic Experimental Methods

Neutron reflection can be done at both pulsed and continuous neutron sources. The only essential differences between them in regard to instrumental technique involve the means by which neutrons of different wavelengths are utilized and identified. With pulsed sources, the broad spectrum of wavelengths present in each pulse can be used because, for elastic scattering, the wavelength distribution of the beam can be determined by time-of-flight measurement. For continuous sources, a relatively narrow band of wavelengths, as defined by a crystal monochromator, is typically employed. The discussions

to follow assume a continuous beam; for the most part, however, the experimental methodology described is applicable to pulsed beam reflectometers as well.

Another relatively general classification of neutron reflectometers can be made. For studying interfaces between solid and another solid, fluid, or gas, a sample can be oriented with its reflecting surface(s) vertical (and with the scattering plane, as defined by nominal incident and reflected wavevectors, horizontal). On the other hand, practical study of gas-fluid interfaces needs the liquid to be horizontal. The primary difference between these two types of reflectometers involves the mechanisms employed to direct the incident beam onto the sample and subsequently detect the reflected beam. For the sake of conceptual simplicity, we will assume the reflecting surface(s) of the sample to be vertical so that the nominal direction of the incident beam remains fixed relative to its source. Again, this choice does not limit, in any essential way, the relevance of the discussion to the one configuration.

3.1 Instrumental Configuration

Figure 7 is a schematic diagram of a typical neutron reflectometer, which is representative of the NG-1 reflectometer at the NIST Center for Neutron Research. The polarizing and spin flipping devices shown can be ignored for the present discussion, but are essential for magnetization depth profile measurements performed with polarized beams [32]. Within the core of the reactor, neutrons are produced by nuclear fission. The relatively high energies of these neutrons are subsequently moderated by collisions with heavy water at room temperature, resulting in a characteristic distribution of wavelengths with a peak in *elastically reflected intensity* (for $Q = 0.1 \text{ \AA}^{-1}$, and $\Delta Q/Q = 0.05$) occurring at a wavelength about 1.5 \AA . The energy distribution is further moderated by the liquid hydrogen "cold source", shown schematically in Fig. 7, shifting the peak in elastically reflected intensity to approximately 5 \AA . The beam of cold neutrons is transported through an evacuated rectangular guide, the smooth, flat interior walls of which are coated with a Ni film which gives a relatively large critical angle for total external or mirror reflection of about 0.1 deg per \AA of incident wavelength.

This beam then impinges upon a pyrolytic graphite monochromating crystal array which Bragg reflects a vertically focussed beam onto the sample. The (002) atomic planes of the graphite crystal reflect a beam with a nominal wavelength $\lambda = 4.75 \text{ \AA}$ for the chosen 90° scattering angle $2\theta_M (\lambda = 2d \sin \theta_M)$, where d is the (002) atomic plane spacing, approximately 3.354 \AA , and θ_M is the glancing angle of incidence measured from the crystal surface. The pyrolytic graphite consists of microcrystallites, which are essentially perfect single crystals of hexagonally arrayed carbon atoms, having dimensions of hundreds to thousands of \AA , both along the (002) direction and perpendicular to it.

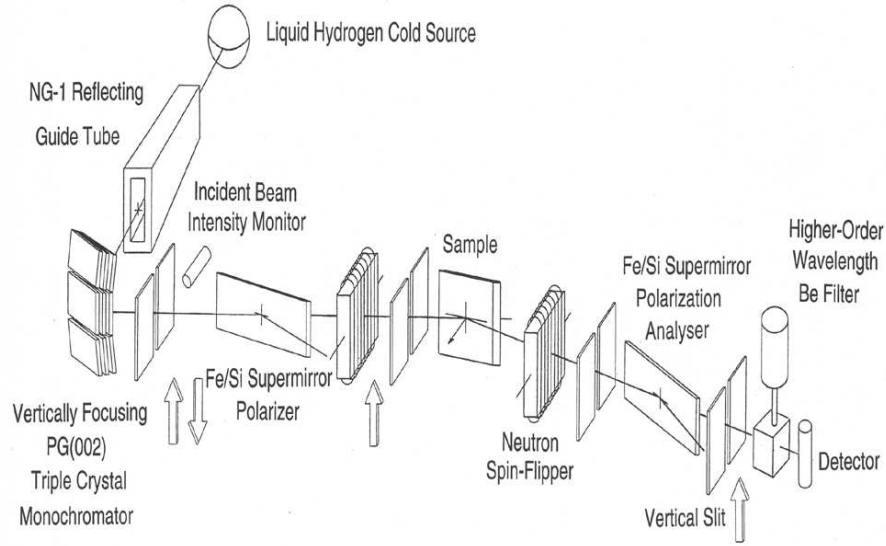


Fig. 7. Schematic of a typical neutron reflectometer (representative of the NG-1 polarized beam reflectometer at the NIST Center for Neutron Research; the polarizing and spin flipping devices are used in the determination of the vector magnetization depth profile in magnetic films and can be ignored for this presentation).

The beam reflected onto the sample by the monochromating crystal has a wavelength distribution determined mainly by the angular distribution of neutrons within the guide, the FWHM of the angular distribution of the graphite crystal's mosaic blocks, the interplanar spacing of the (002) graphite atomic planes, and the horizontal angular collimation of the beam (defined by the pair of vertical slits preceding the sample, as shown in Fig. 7.) A typical horizontal angular divergence is between 1 min and 10 min of arc, and because this is relatively small compared with that in the guide and the crystal mosaic angular spread, the wavelength resolution, $\Delta\lambda/\lambda$, principally depends on the latter two fixed quantities and is about 1 %.

As pictured in Fig. 7, each finger of a vertically focusing monochromator array is a stack of several graphite crystals, slightly inclined relative to one another, so as to create a broader (but effectively anisotropic) mosaic, thereby widening the wavelength band (to increase the intensity within the limits allowed by a given Q -resolution). At the NCNR NG-1 reflectometer, the 15 cm beam height in the guide is focused down to about 3 cm at the sample position so that the vertical angular divergence is approximately 2.5° . For specular

reflectivity measurements, this relatively relaxed vertical angular divergence has a negligible effect on the Q -resolution.

Downstream of the sample position is a second pair of slits before the detector which are primarily used to suppress incoherent scattering background. For specular reflectivity measurements, the wavelength distribution and angular divergence of the incident beam, in conjunction with the glancing angle of incidence that the beam makes with the surface of a flat sample, determine a nominal value of Q and its associated resolution width. In addition, the slit just before the detector is needed to properly shape the instrumental resolution function in performing nonspecular scattering scans perpendicular to the specular direction. In the latter case, the slit before the detector is significantly narrowed as the sample angle is rotated with the detector at a fixed scattering angle (this results in a trajectory in reciprocal space that is nearly orthogonal to the specular direction for sufficiently small angles). For a sample that is distorted enough from perfect flatness, slits following the sample may block contributions to the reflected intensity from certain distorted regions of the sample surface from reaching the detector, thereby effectively improving the Q -resolution for specular reflection.

3.2 Instrumental Resolution and the Intrinsic Coherence Lengths of the Neutron

The theory of neutron reflection discussed in Sec. 2 assumed that each neutron in a beam of noninteracting, independent particles could be described by a single plane wave of infinite spatial extent. Generally, a neutron is more accurately described as a superposition of component plane waves, commonly known as a wave packet [13]. The wave packet description follows from localization of the neutron in space and imparts characteristic *coherence lengths*, both parallel and perpendicular to the direction of propagation defined by a nominal neutron wavevector \mathbf{k} . These lengths—a measure of the combined uncertainties in position and momentum that must be associated with an individual neutron—determine the effective volume of the scattering medium with which the neutron wave packets *coherently* interact, and, consequently, they are important to interpreting specular reflectivity data. However, because the neutrons constituting the incident beam originate from different, uncorrelated points within the source, there is an additional component of uncertainty in a distribution of nominal neutron wavevectors. This *incoherent* component can dominate the coherent, wave-packet-spread component, ultimately leading to the familiar “instrumental resolution” distribution in Q . In-depth, quantitative treatments of neutron coherence and instrumental resolution are given in several places [33, 34, 35, 36, 37, 38]. Nonetheless, it is worthwhile here to consider these points further, at least qualitatively.

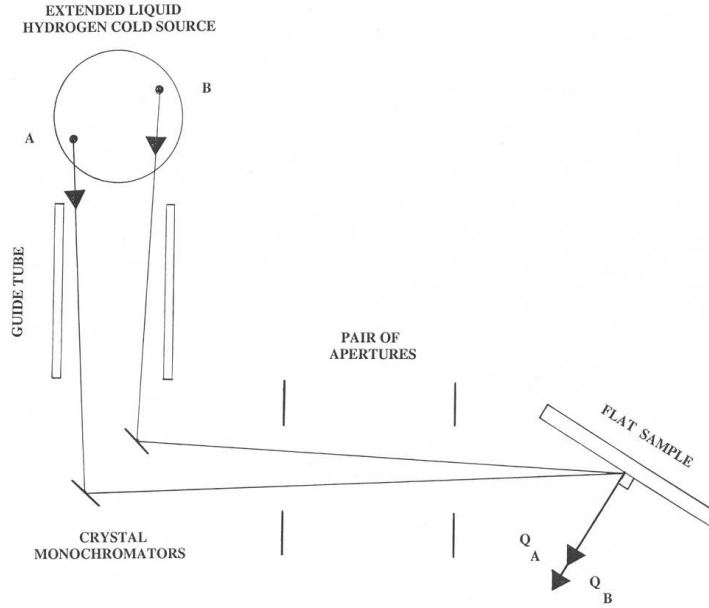


Fig. 8. Schematic representation of two independent, noninteracting neutrons, "A" and "B", emanating from different places in the cold source and passing through common instrumental optical elements en route to the sample. The size and shape of the wave packet describing neutron A is similar to that of B, but each packet has a different nominal wavevector direction. See the discussion in the text regarding coherent vs. incoherent components of the effective instrumental resolution.

3.3 Incoherent versus Coherent Effects

Figure 8 shows a liquid hydrogen moderator which acts as an incoherent source of neutrons for a specular reflectivity experiment to be performed downstream in a geometrically well-defined beam. Each of two neutrons, "A" and "B", radiates from a separate region of the liquid hydrogen cold source, as a result of an incoherent scattering event involving a single hydrogen nucleus. In general, all the coherent interactions of either neutron with objects along its path to the sample—*e.g.*, the guide walls, a particular monochromator microcrystallite, and the pair of rectangular apertures preceding the sample—contribute to redefining the size and shape of the wave packet representing that neutron when it eventually encounters the sample. Nonetheless, let us assume that neutrons A and B are represented by wave packets of the same size and shape. Each neutron wave packet then possesses the same characteristic coherence lengths related to the uncertainties in position ($\Delta x, \Delta y, \Delta z$) and wavevector ($\Delta k_x, \Delta k_y, \Delta k_z$) of the neutron, that, as mentioned above, define a volume

over which the neutron interacts with the sample. Any size and shape wave packet is an appropriately weighted superposition of plane waves [13]. The two neutrons travel in different directions, defined by their nominal wavevectors, so that each neutron is Bragg reflected from a separate monochromator crystal segment (but through the same pair of apertures) onto the sample. The latter fact means that the values of the normal component of the incident wavevector $k_{0z} = Q/2$ for the two neutrons differ from one another.

For specular reflection, we need only consider the z -axis normal to the plane of the film. In practice, at a continuous source, specular reflection measurements are performed with neutrons having nearly the same nominal k_0 incident at different glancing angles θ , so that the resulting range of $k_{0z} = k_0 \sin \theta$ values are obtained by changing the angle of incidence. Then, the relevant longitudinal coherence length effectively is the projection of the neutron wave packet coherence length along z . (See [39] for the case of normal incidence with ultra-cold neutrons.) The reflectivity, $|r|^2$, which results for a single plane wave incident on a perfectly flat and homogeneous Ni film 1000 Å thick is plotted in Fig. 9. As is well-known, the oscillations evident in Fig. 9, the so-called "Kiessig fringes", are produced by interference between parts of the wave that are scattered from front and back film surfaces; the period of the oscillations is approximately $2\pi/L$. Such interference requires that the incident plane wave interact with both interfaces "coherently", *i.e.*, simultaneously.

For a one-dimensional incident wave packet with a finite characteristic coherence length along the z -axis eq. 1 must be solved. We can describe the incident wave function as a wave packet $\psi_{\text{WP}}(z)^{\text{coh}}$ consisting of a superposition of plane waves, each component having a well defined value of k_z , *viz.*,

$$\psi_{\text{WP}}^{\text{coh}}(z) = \int_{-\infty}^{\infty} \phi(k_z|k_{0z}) e^{ik_z z} dk_z \quad (16)$$

where the normalized weighting $\phi(k_z|k_{0z})$ might, for instance, be represented by a Gaussian distribution centered on the nominal k_{0z} , *viz.*,

$$\phi(k_z) = \frac{2}{\Gamma_{\text{coh}}} \sqrt{\frac{\ln 2}{\pi}} e^{\frac{-4 \ln 2}{\Gamma_{\text{coh}}^2} (k_z - k_{0z})^2}, \quad (17)$$

where Γ_{coh} is the FWHM of the distribution. For such a Gaussian wave packet, the relationship between uncertainties Δk_z and Δz of wavevector and position, respectively, along z is given by the Heisenberg uncertainty relation

$$\Delta z \Delta k_z = \frac{1}{2}. \quad (18)$$

Although we will not explicitly solve the wave equation for the case of an incident wave packet here, let us call the result of that calculation for the reflection amplitude $r_{\text{WP}}^{\text{coh}}(k_{0z})$, where k_{0z} denotes the nominal k_z for the wave packet. To a first approximation, $r_{\text{WP}}^{\text{coh}}$ is a superposition of "components"

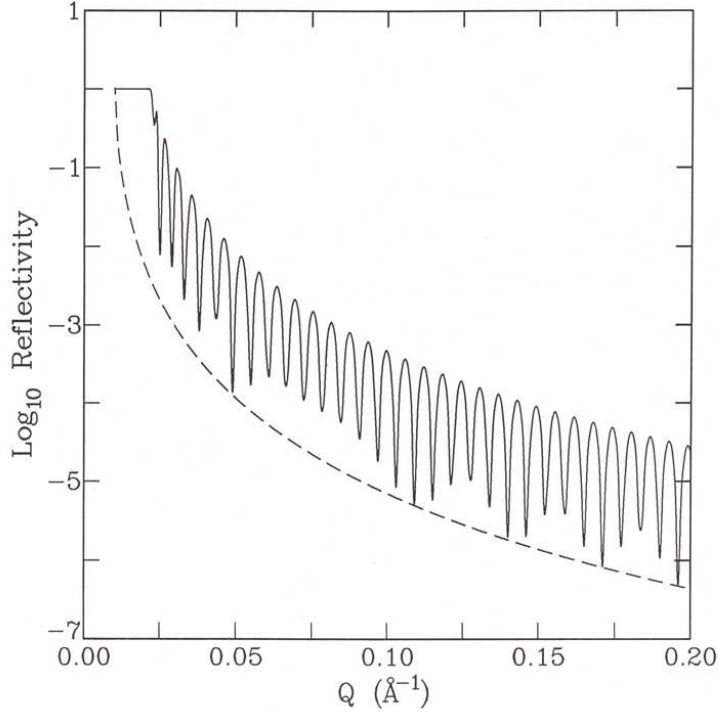


Fig. 9. Specular neutron reflectivity for a free-standing Ni film, 5000 Å thick. The oscillations are a result of the interference which occurs in the simultaneous scattering of the wave from front and back surfaces of the film, as discussed in the text. The period of the oscillations is approximately $2\pi/L$.

$r(k_z)$ with the same weighting $\phi(k_z|k_{0z})$ as in eq. 16. The resulting specular reflectivity for the case where the incident neutron is described as a wave packet with a coherence length $L' \ll L$ along z does not display the pronounced Kiessig fringes appearing in Fig. 9 because the degree to which the neutron can coherently interact with front and back surfaces is significantly diminished.

Let us now consider a collection of neutrons which constitute an incident beam. Let us assume that every neutron in the beam is described by the same one-dimensional wave packet and coherence length, but that there now exists a distribution of different nominal wavevector magnitudes, k_{0z} , distinct from the distribution of k_z about a given k_{0z} in a wave packet. We can, for convenience, choose this distribution also to be Gaussian. However, the distribution of k_{0z} describes an incoherent association of our "test" neutrons A and B, in the sense that each neutron in the beam reflects from the film

independently. Thus, the *measured reflectivity* $R_M(Q_M)$, at nominal $Q = Q_M$, for an incident beam of such neutrons is the average over $Q = 2k_{0z}$ of the wave packet reflectivities $|r_{WP}^{coh}(Q)|^2$; *viz.*,

$$R_M(Q_M) = \frac{2}{\Gamma_{inc}} \sqrt{\frac{\ln 2}{\pi}} \int_{-\infty}^{\infty} |r_{WP}^{coh}(Q/2)|^2 e^{-\frac{4 \ln 2}{\Gamma_{inc}^2} (Q - Q_M)^2} dQ, \quad (19)$$

where Γ_{inc} is the FWHM of the Q -distribution. The convolution in eq. 19 is the "instrumental resolution" commonly employed—but usually with r_{WP}^{coh} replaced by r for the ideal case of an incident plane wave—and also contributes to smearing the fringes in Fig. 9. Thus, instrumental resolution should be as tight as reasonably possible, especially where eventual knowledge of r_{WP}^{coh} is the goal of the measurement.

Thus, the source of the neutrons and their interactions with instrumental components, which combine to define the size, shape and direction of each neutron wave packet, determine both coherent and incoherent distributions of possible wavevector components in the measurements. The coherent contribution characterizes the wave packets describing individual neutrons, our A or B, while the incoherent contribution emanates from the pathways taken by different neutrons, A *and* B. For example, diffraction by a sufficiently narrow slit aperture may significantly distort the nominal neutron plane wave, leading to a coherent distribution of wavevectors (common to A and B), while the mosaic structure of the monochromator induces an incoherent spread of wavevectors incident on the sample, distinguishing A from B.

3.4 In-plane Averaging

In-plane structure causes non-specular reflection, as previously mentioned, but even when this is weak enough to be ignored, the observed specular reflection will be influenced by lateral variations of the depth profile. The common assumption is that the laterally averaged scattering length density produces the specular "component" of reflection. That is, if the SLD profile is described everywhere in the film by $\rho(x, y, z)$, then the reflection amplitude $r(Q)$ is caused by its lateral average $\rho(z) = \langle \rho(x, y, z) \rangle_{xy}$, as introduced in eq. 2 and the related discussion. This can be true, however, only to the extent that the neutron beam is laterally coherent over the surface of the film, so that such an average is meaningful.

In three dimensions, we can ascribe two coherence lengths to the incident neutron wave packet: a longitudinal coherence length ℓ_z^{coh} , which is the coherence length we had in mind in discussing the immediate implications of eq. 18 in terms of film thickness; and a lateral or in-plane coherence length ℓ_{xy}^{coh} , which limits the size of the surface the incident wave packet "coherently sees." Note that the coherence lengths discussed here are the projections of the neutron wave packet coherence lengths, parallel and perpendicular to its nominal wavevector, projected onto the coordinate axes of the sample.

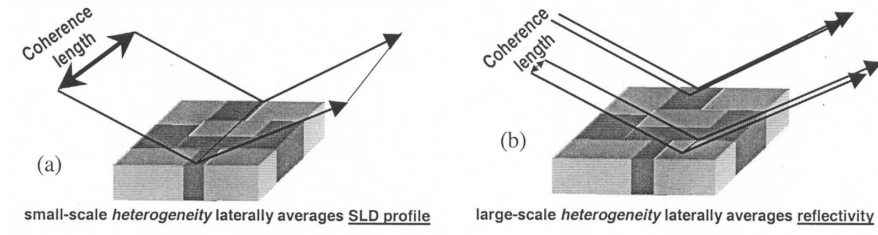


Fig. 10. Schematic representation of neutron coherence length and in-plane dimensions of homogeneous sample areas.

Now in eq. 19 we implicitly assumed that the film was laterally homogeneous. More generally, however, the reflectivity $|r_{\text{WP}}^{\text{coh}}|^2$ appearing in the "incoherent" convolution integral must be replaced by a lateral average $\langle |r_{\text{WP}}^{\text{coh}}|^2 \rangle_{xy}$. For example, a sample characterized by partial coverage might comprise a film composed of two (fully and partially covered) components and a corresponding scale of inhomogeneity ℓ_{xy} equal to the larger of the dimensions associated with the fully and partially covered regions. In cases where $\ell_{xy}^{\text{coh}} \gg \ell_{xy}$, the film appears to the neutron beam as homogeneous, and the specular reflectivity is caused by the corresponding lateral average, $\langle \rho(x, y, z) \rangle_{xy}$, as in eq. 2. However, when $\ell_{xy}^{\text{coh}} \ll \ell_{xy}$, the film appears, instead, as a collection of several types of films, each of which reflects the neutrons according to their "local" $\rho(z)$. Then the measured reflectivity is an areally weighted average of reflectivities from several different films. That is,

$$\langle |r_{\text{WP}}^{\text{coh}}|^2 \rangle \simeq \begin{cases} |r_{\text{WP}}^{\text{coh}}|^2, & \text{for } \ell_{xy}^{\text{coh}} \gg \ell_{xy} \\ \sum_j w_j |r_{\text{WP},j}^{\text{coh}}|^2, & \text{for } \ell_{xy}^{\text{coh}} \ll \ell_{xy}, \end{cases} \quad (20)$$

where w_j is the weighting for the j -th type of in-plane component. In the second case, unlike the first, there is no corresponding physically defined $\rho(z)$, so any attempt to analyze the reflectivity in terms of "the" SLD profile that produced it must fail, unless $w_J \approx 1$ for some $j = J$.

Thus we must ask, how do we know which case of eq. 20 is the correct one for a given experiment? In some cases a visual inspection of the sample may suffice to say; if we can literally see, *i.e.*, with visible light, evidence for lateral homogeneities much greater than the neutron coherence length, then the much shorter wavelength neutron beam can "see" it too. However, a film may appear visibly homogeneous while still behaving as if $\ell_{xy}^{\text{coh}} \ll \ell_{xy}$ and thus acting as an inhomogeneous collection of reflectors.

Now consider the specific case in which regions of two different SLDs are distributed within the plane of the film as shown in Fig. 10a and 10b. If the linear dimensions of the area of either SLD is much smaller than the in-

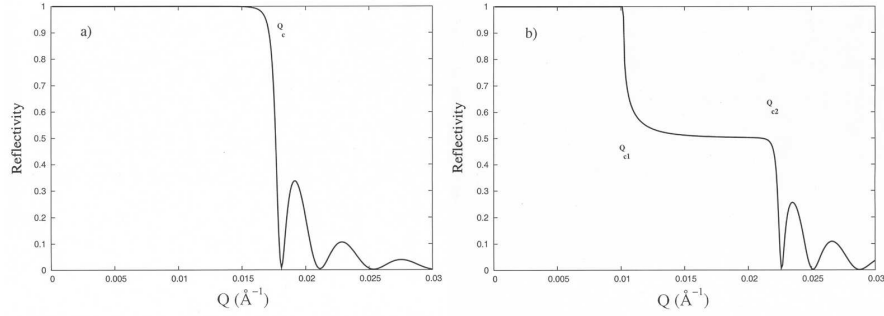


Fig. 11. Specular reflectivity: a) corresponding to picture in Fig. 10a; and b) corresponding to picture in Fig. 10b; it is assumed that the two different SLDs cover equal areas in both cases.

plane projection of the neutron coherence length, as schematically represented by the straight line in Fig. 10a, then the neutron wave effectively averages over the SLDs of the two regions; *i.e.*, the measured specular reflectivity is that for the areally weighted average, as plotted in Fig. 11a. However, if the linear dimensions of either SLD component are much larger than the in-plane coherence length, the measured reflectivity is the incoherent sum of two areally weighted reflectivities, as in eq. 20, each corresponding to one region of SLD, as plotted in Fig. 11b (assuming equal weightings). This suggests that use of samples with known in-plane SLD distributions, such as might be fabricated by lithographic techniques, could be used to infer neutron coherence lengths independently, to some degree, of the incoherent instrumental resolution.

In typical reflectometer configurations, similar to those discussed above for specular measurements, except for a tighter horizontal aperture in front of the detector, it is possible, by observing non-specular reflection at low Q_z , to resolve in-plane structures, *e.g.*, lithographically patterned surfaces, with dimensions of tens of microns. Indeed, the rulings of optical diffraction gratings can be measured with neutron reflectometry.

3.5 Q -Resolution for Specular Reflectivity, Assuming an Incoherent Beam

It is instructive and practical to consider the common situation where the wave packets are well approximated by ideal plane waves (wave packets having a very narrow distribution of wavevectors), so that resolution in fact is dominated by an incoherent distribution of mean wavevectors. The instrumental Q -resolution for specular reflection is then determined by applying the simple laws of geometrical optics for reflection and refraction to the reflecting guide, the mosaic crystal monochromator (for which Bragg's law is also imposed), the pair of slits preceding the sample, and the surface of the

sample itself (since the flatness of the sample also affects the measured value of Q).

Figure 12 resolves the incident and reflected wavevectors, \mathbf{k}_i and \mathbf{k}_f , respectively, into their rectangular components. From the diagram we can write

$$\begin{aligned} k_{\mu x} &= k \cos \alpha_\mu \cos \theta_\mu \\ k_{\mu y} &= k \sin \alpha_\mu \\ k_{\mu z} &= k \cos \alpha_\mu \sin \theta_\mu \end{aligned} \quad (21)$$

where $\mu = i, f$ and $k = 2\pi/\lambda$. For specular reflection $\theta_i = \theta_f$, and, given that α typically is at most a few degrees, the expression for Q (*i.e.*, $Q = -Q_z = k_i - k_f$, as defined in the Introduction) reduces, to a good approximation, to the familiar

$$Q = 2k \sin \theta. \quad (22)$$

In terms of wavelength λ and the grazing angle θ , the fractional uncertainty in Q then is

$$\frac{\delta Q}{Q} = \frac{\delta \lambda}{\lambda} + \frac{\delta \theta}{\tan \theta}, \quad (23)$$

which, for the typically small angles in reflectivity experiments, is approximately

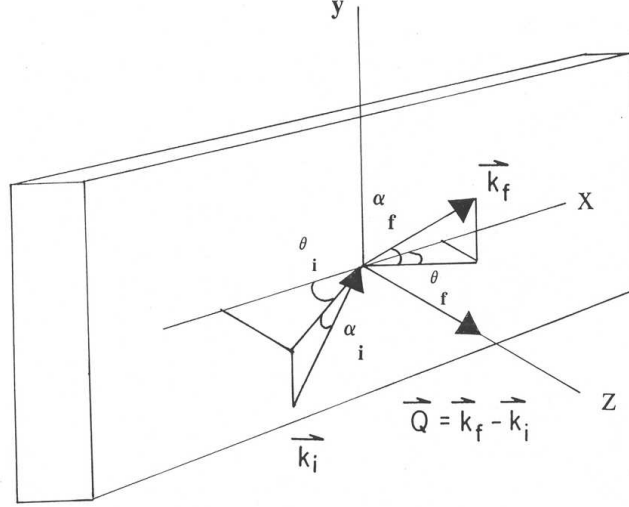


Fig. 12. Incident and reflected neutron wavevectors resolved into their respective rectangular components.

$$\frac{\delta Q}{Q} \approx \frac{\delta \lambda}{\lambda} + \frac{\delta \theta}{\theta}, \quad (24)$$

since $\tan \theta \approx \sin \theta \approx \theta$. As mentioned earlier, the angular divergences of the beam impinging on the monochromator crystal and the monochromator's mosaic distribution are normally significantly greater than the divergence defined by the slits which determine $\delta \theta$. In this case the fractional wavelength uncertainty is nearly independent of θ , and the two contributions to the fractional uncertainty in Q can be taken to be independent, so that

$$\frac{\delta Q}{Q} \approx \sqrt{\left(\frac{\delta \lambda}{\lambda}\right)^2 + \left(\frac{\delta \theta}{\theta}\right)^2}. \quad (25)$$

Usually in specular reflectivity measurements, the slits preceding the sample are opened proportionally with θ , once the sample has fully intercepted the entire width of the incident beam, so that $\delta Q/Q$ (as well as the "footprint" of the beam on the sample) remain approximately constant with θ and Q (in the small angle approximation). A typical value of $\delta Q/Q$ is 0.025.

3.6 Measurement of the Reflectivity

To obtain the specular reflectivity, the reflected intensity is first measured as a function of wavevector Q —at a continuous source, by varying the incident angle θ at fixed wavelength and using eq. 22—up to a maximum value Q_{\max} at which the signal to noise ratio S/N becomes prohibitively low. Background from incoherent scattering within the sample, substrate or surrounding media, as well as from external sources must be measured and then subtracted from the measured reflected intensity. The resultant signal next must be divided by the incident beam intensity (which is also a function of θ if the slits are opened with increasing reflection angle). Corrections to the reflectivity spectrum also must be applied at values of Q below which the sample does not fully intercept the width of the incident beam (the so-called "footprint" correction). Finally, at least in principle, the instrumental resolution function needs to be deconvolved from the measured reflectivity data, at least when the resolution correction is significant enough to warrant it. However, in practice this rarely is done because deconvolution is a mathematically problematic operation on finite data sets. In the following subsections, some of the practical aspects of data reduction are discussed.

3.7 Sample Alignment

In order to obtain quantitatively accurate reflectivity data, proper sample alignment is essential. The procedure for accomplishing this is straightforward but can be complicated by substrates deformed from perfect flatness. The goal is to align the sample surface such that it is parallel to and bisects the width of

the incident beam, viewed as a ribbon. (It is presumed that the centers of the beam and sample surface coincide.) A rough orientation of the sample can be obtained optically by translating the reflecting surface close to the center of the beam defined by the slit apertures and rotating the sample to be parallel with the beam. Any angular tilt of the sample away from vertical, about the horizontal axis of the incident beam, can be eliminated either using a laser beam reference or even a mechanical plumb line.

Then, the detector can be set at zero scattering angle (for specular reflection, the detector is always positioned at a scattering angle twice the reflection angle of the beam relative to the sample surface) with the pair of slits preceding the sample set so that the horizontal divergence is relatively tight, of the order of a minute of arc. The slit immediately following the sample can be set wide enough to accept the entire divergent width of the beam, but the last slit before the detector should be set to a width comparable to that of the first two slits in order to be sensitive to rotations of the sample. The sample is then translated across the incident beam in a scan in which the transmitted intensity is measured at each step. Once the translational position of the interface is located, the sample is rotated in θ at this position with the detector still at zero scattering angle. The occurrence of a central peak corresponds to the position of the sample face being approximately parallel to the incident beam; regions of minimum intensity on either side correspond to the incident beam being reflected by the surface of the sample at a finite scattering angle (and, therefore away from the detector which is at zero scattering angle). The two-step procedure just described can be repeated iteratively until convergence.

With the nominal zero of the sample angle θ defined, the sample can be rotated to a finite angle corresponding to a Q of 0.005 \AA^{-1} ($\theta \approx 0.1^\circ$ for $\lambda = 4.75 \text{ \AA}$) with the detector at twice that angle (slit apertures unchanged). Now a sequence of three scans can be performed: a rotation of the sample in θ (about the vertical axis through the sample surface), referred to as a "rocking" curve; a translation of the sample through the incident beam; an angular tilt of the sample about a horizontal axis through the center of the sample surface. This sequence of scans is performed iteratively until convergence of the sample rotation (to a peak position in θ that occurs at half the scattering angle), translation, and tilt angle are each achieved. This process can also be carried out at negative reflection and scattering angles, which corresponds to the beam being incident from within the substrate (which is possible for the case of a single crystal Si substrate which is highly transparent to neutrons). Although no critical angle for total reflection may exist in going from the denser (Si) medium to air for certain films on the surface, the reflectivity is typically high enough.

A flat sample surface should result in a smoothly shaped rocking scan curve resembling a Gaussian with a FWHM close in value to the angular divergence defined by the pair of slits upstream. Any significant deviation from this (assuming that the tilt was properly optimized), especially manifest

as asymmetric or multiple peak shapes, is indicative of a non-flat sample surface. As already discussed, a non-flat surface results in a broadened Q -resolution which must be accounted for. If the broadening is acceptable, in terms of resolution, precaution must still be taken that the slits downstream of the sample open sufficiently to fully accept the increased divergence of the specularly reflected beam on its path to the detector. This can be accomplished in a straightforward manner by measuring the reflected intensity at a given θ as a function of slit opening until a plateau is achieved. If a critical angle exists for the sample being examined, it also is prudent to perform a longitudinal scan (i.e., the specular θ - 2θ scan) through the critical edge. If the sample is long enough, then a plateau should be reached, below the critical angle, where the reflectivity is practically unity.

3.8 Geometrical Beam Footprint Correction

If the sample is not long enough at lower reflection angles to fully intercept the full width of the incident beam, a decreased reflectivity occurs. If the sample has a critical angle, θ_c , above the point at which the surface intercepts the full width of the incident beam, then the correction below that point is trivial; the reflectivity simply is defined as unity for $0 < \theta \leq \theta_c$. However, if a critical angle is too small or nonexistent, then another sample of the same size, but with a critical angle that lies above the point of full interception, can be measured under identical conditions to obtain the proper geometrical scaling as a function of glancing angle. However, if the sample is not flat enough, an accurate footprint correction may not be achievable.

3.9 Material Fronting Medium and Beam "Side" Entry

Taking advantage of the near transparency to neutrons of Si, sapphire, or quartz single crystals, the reflectivity of films deposited on such substrates can be measured with a beam incident upon the film from within the substrate. This makes it possible for a film of interest to be in contact with a neutron-attenuating aqueous reservoir or other fluid medium, as shown in the following subsection on cell design. In practice, incidence from within a substrate typically requires the beam to enter through a surface of the substrate perpendicular to the film, *i.e.*, through a side of the crystal, as shown in Fig. 13. The beam incident from vacuum on the left enters the fronting medium (single crystalline Si, for example) through a face which is perpendicular to the plane of the film. The regions about the side boundary face and the film surface (schematically indicated in the figure by the rectangular perimeters in the figure) are assumed to be sufficiently separated that the neutron wave packet does not interact with both interfaces simultaneously. As described in the Introduction, for vacuum fronting, the value of the wavevector transfer $2k_z$ in specular reflection, as measured in the laboratory, satisfies

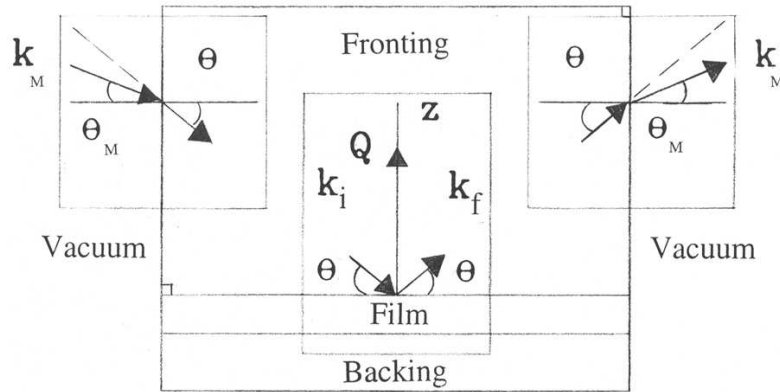


Fig. 13. Side-entry geometry typically employed in the case of a beam incident through material (non-vacuum fronting).

$$2k_z = |\mathbf{k}_f - \mathbf{k}_i| = 2k_M \sin \theta_M = 2k_{0z} = Q. \quad (26)$$

Here the subscript M denotes quantities measured on the instrument in the laboratory, as indicated in Fig. 13 (since, for vacuum, there is no side interface to cross through). On the other hand, for nonvacuum fronting, a refractive bending occurs as the neutron crosses the side boundary, which, from Snell's law, is

$$\sin \theta_{\text{M}} = n_f \sin \theta \quad (27)$$

where n_f is the refractive index of the fronting medium

$$n_f = \sqrt{1 - \frac{4\pi\rho_f}{k_M^2}}, \quad (28)$$

where $\rho_f = \rho^I$. The index of refraction is not to be confused with n_z^I , defined in eq. 4. Using eq. 27, the value of k_z *inside* the fronting medium then is

$$k_z = k \sin \theta = k_{\text{M}} n_f \frac{\sin \theta_{\text{M}}}{n_f} = k_{\text{M}} \sin \theta_{\text{M}}. \quad (29)$$

The value of k_z in the fronting is the value k_{Mz} measured on the instrument by measuring θ_M and by computing $k_M = 2\pi/\lambda$. However, according to the 1-D description in eq. 1, for a given k_{0z} , the wavevector incident on the film is k^I of eq. 4, as if side entry of the incident beam had not occurred. Therefore, to adapt eq. 1 to side entry, its wavevector *parameter* k_{0z} , or the corresponding Q , must be identified in terms of the *measured* k_z , as given in eq. 29. With eq. 4 and eq. 29

$$k_z^I = \sqrt{k_{0z}^2 - 4\pi\rho_f} = \frac{2\pi \sin \theta_M}{\lambda}, \quad (30)$$

so that, solving for k_{0z} ,

$$Q = 2k_{0z} = \sqrt{\left(\frac{4\pi \sin \theta_M}{\lambda}\right)^2 + 16\pi\rho_f}. \quad (31)$$

Therefore, for nonvacuum fronting and with side entry, in comparing the reflectivity measured at an angle θ_M to a reflectivity calculated for a model SLD profile, the value of Q at which the theoretical expression for $r(Q)$ (or $|r(Q)|^2$) must be computed is given by eq. 31.

3.10 Sample Cell Designs with Liquid Reservoirs

In the study of biomimetic films, it is often required that the film be in contact with an aqueous reservoir. As already discussed, the high transparency of neutrons through single crystalline materials such as Si, Al_2O_3 , and SiO_2 make it possible to construct fluid cells in which the single crystal serves both as substrate and fronting medium for the neutron beam. In principle, the design of a fluid cell is straightforward but, as is discussed in the following section, contributions to the background from the media surrounding the film can be the predominant factor which limits the maximum Q at which the reflectivity can be measured and, consequently, the spatial resolution of the SLD depth profile.

Figure 14 shows face and end-on views of a liquid cell that has evolved as a standard piece of equipment for reflectivity measurements. The single crystal fronting and backing are assembled from 7.62 cm diameter discs of various thicknesses. Under the correct conditions, to be described below, such a cell, in which the incident, transmitted and reflected neutron beams in the vicinity of the sample are entirely within the single crystal media, typically allows maximum Q in the range $Q_{\max} \approx 0.3 \text{ \AA}$ to $Q_{\max} \approx 0.4 \text{ \AA}$. The single crystal discs are normally polished on one side. Note that the sample may be deposited on a thinner disc, e.g., 4.7625 mm, in contact with a thicker Si piece; the relatively thin air gap in between produces no significant effect on the measured reflectivity for such thicknesses. The thickness of the reservoir next to the film is defined by an annular gasket (e.g., nitrile or other similarly impervious material). This dimension can be as small as about $25 \mu\text{m}$ without any significant effect on the measured film reflectivity from the face of the backing crystal, but for reservoirs that are too thin, the possibility of coherent contributions from the face of the backing crystal needs to be considered. Naturally, the fronting and backing crystals must be sufficiently thick to fully accommodate incident and reflected beam widths at the maximum reflection angle. Fluid is introduced through a hole (e.g., ultrasonically drilled through the single crystal Si or Al_2O_3 and of diameter 1 – 2 mm) near the bottom of

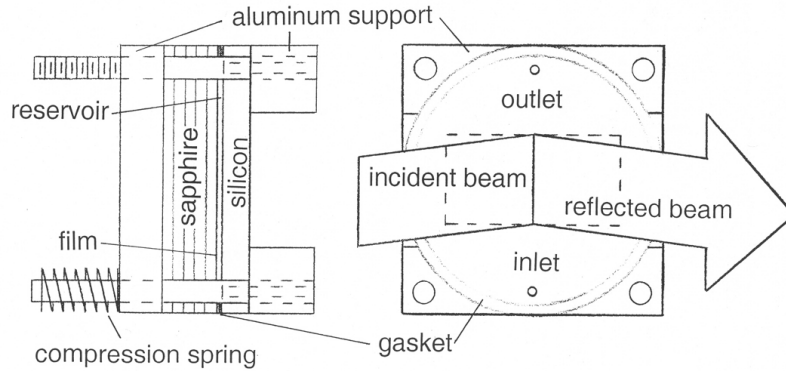


Fig. 14. Schematic views, face- and end-on, of fluid reservoir cell used in neutron reflectivity measurements as described in detail in the text.

the backing disc; a similar hole diametrically opposed at the top of the disc serves as an outlet. The horizontal slits preceding the sample are continuously adjusted throughout the specular scan to maintain a constant footprint. A cylindrical "top hat" made of aluminum can be placed around the sample and the volume surrounding the cell filled with argon gas, which scatters neutrons significantly less than air. Brass or copper heating/cooling blocks can be attached to the aluminum cell frame at top and bottom. Temperature control (over a range from about -10 C to 80 C) can be maintained by a combination of fluid flow through the blocks and electrical resistance heater cartridges.

It is difficult to overemphasize the importance of using substrates that have been polished smooth and flat and of maintaining flatness in the compressed sandwich of the cell. A root mean square (RMS) roughness about 3 – 5 Å is obtainable and desirable since this ultimately limits the spatial resolution in the measured SLD depth profile. Flatness, on the other hand, as commonly used, is associated with in-plane areas comparable to or greater than the coherence length (of order micrometers); the normals to these areas should not deviate more than about 0.01° from the nominal direction. As discussed earlier, deviations from perfect flatness also degrade the effective instrumental Q -resolution for specular reflection measurements.

For a lipid bilayer on a Au film (thickness ≈ 100 Å) deposited on a 0.5 mm thick Si substrate and placed next to a D₂O reservoir of thickness ≈ 25 μm (in this case defined by a gasket and another 0.5 mm Si crystal as backing), specular neutron reflectivities have been measured for $Q_{\max} = 0.73$ Å⁻¹ [40].

If the sample film can be exposed to a humid atmosphere instead of an aqueous reservoir (*e.g.*, water vapor in Ar), then it is advantageous for reduction of background to deposit the film of interest on a thin (*e.g.*, 0.5 mm) single crystalline substrate. The humidity can be controlled either by saturated salt solutions or mechanical humidity generators.

3.11 Sources of Background

Normally, a single lipid bilayer membrane is itself a negligible source of incoherent scattering background. For a well-shielded instrument, external sources of background can also be relatively insignificant. The major contribution to the background in a specular reflectivity measurement most often originates in the media surrounding the film which is exposed to an incident beam that can be relatively intense at larger Q -values, where the slits are opened wide. For polycrystalline substrates, even though the wavelengths are often long enough that no Bragg scattering can occur (*e.g.*, aluminum at $\lambda = 5.0$ Å), small angle scattering from the crystal grains, as well as incoherent and inelastic scattering, can contribute. Single crystalline substrates can produce a significant amount of incoherent and inelastic scattering, as well, but are usually preferred to polycrystalline or amorphous (*e.g.*, glass) materials. If the substrate contains a neutron absorber, *e.g.*, boron in pyrex glass, the scattering that contributes to the background can be reduced, although the presence of significant absorption requires that the substrate be used only as a backing medium and that an imaginary component of the scattering length density for the substrate be taken into account in the analysis of the measured reflectivity. In any event, one way to judge the potential of a substrate for producing background, absent absorption, is to measure its transmission. Away from the critical angle, specular reflection falls rapidly with Q , at least as fast as Q^{-4} at large Q . Thus, at large Q , most of the beam should be transmitted through the backing with a transmission close to unity. Measuring a reduced value of the transmission, say, about 0.85 for a Si single crystal substrate 7.5 cm thick, implies that a substantial number of non-reflected neutrons are scattered elsewhere, some fraction of which enter the detector as background.

In addition to substrates, an aqueous reservoir adjacent to the sample film can also contribute a substantial amount of incoherent background, especially if it contains H_2O . Where possible, it is advantageous to use D_2O in place of ordinary water and to minimize the reservoir thickness. Note that single scattering of a neutron from a hydrogen nucleus is most often an incoherent event, resulting in an angularly isotropic distribution of scattered radiation.

Even when it is possible to use a thin single crystalline substrate, the air surrounding the sample which is intercepted by the incident and transmitted beams and simultaneously viewed by the detector can be a substantial source of background. This background can be eliminated by placing the sample in an evacuated chamber or by replacing the air with He or Ar gas, which scatter significantly less than nitrogen and oxygen.

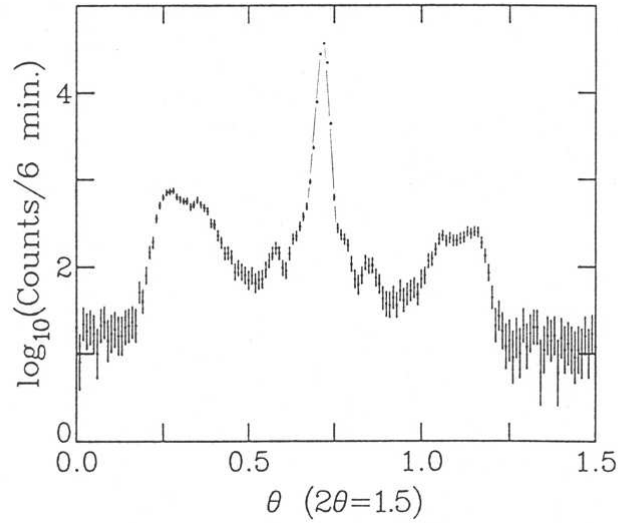


Fig. 15. Plot of intensity vs. rocking angle (θ) at a fixed scattering angle for a multilayer Ni/Ti sample with significant in-plane SLD variations, as described in the text.

3.12 Background Measurement

To measure the background at a given Q , the detector angle 2θ is set close to the specular condition but offset far enough to miss the specular signal. The amount of offset for given slit openings and beam width can be determined by performing a transverse scan along a direction perpendicular to the film normal (z -axis) and with the horizontal width of the aperture in front of the detector sufficiently tight; a rocking curve is normally a satisfactory approximation. Note, in particular, that nonspecular reflection is not background, which is more or less isotropic, but is scattering from in-plane variations in SLD in the sample. As discussed earlier, the observation of significant nonspecular scattering requires proper evaluation of the validity of the use of the one-dimensional specular scattering theory. Fig. 15 is a plot of intensity versus rocking angle θ at a fixed scattering angle for a metallic Ni/Ti multilayered sample having a relatively large number of interfaces with roughnesses that could be correlated from one layer to another, thereby manifesting some degree of three-dimensional order.

3.13 Background Suppression

In our discussion above, we already mentioned that background can be suppressed by using thin single crystal substrates to support the film and to replace the surrounding air with vacuum, He, or Ar gas. It was also mentioned how the pair of slits downstream of the sample have no effect on the specular reflectivity measured from a flat sample. Instead, the slits following the sample act to discriminate the specular reflected signal from signal have a wider angular divergence. However, it can happen that the distance between the two slits which define the incident beam angular divergence is greater than that for the pair of slits which precede the detector. In such a case, opening the slits after the sample just enough to allow the full width of the specularly reflected beam through to the detector can result in a wider angular acceptance than that defined by the incident beam slits. Consequently, more of the isotropic incoherently scattered background is allowed into the detector. To remedy this, a set of parallel channels, called a "Soller" collimator, can be used to accept a wider beam at a narrower angular divergence more closely matched to that of the incident beam. Either a Soller collimator with reflecting partitions or one with non-reflecting, absorbing walls can be employed for the purpose.

Alternatively, a mosaic crystal with an appropriate angular distribution of mosaic blocks can be used to discriminate against a more widely divergent incoherent background. Unfortunately, a Soller collimator or analyzer crystal produces transmission and reflectivity losses for the specular signal, which typically range between 20 % and 50 %. Therefore, proper analysis of the signal to noise ratio, including efficiency, counting statistics, and error propagation considerations, is required for the proper use of these devices.

3.14 Signal Enhancement

To improve the signal to noise ratio, it can be important to boost the signal, as well as reducing the background. One method of signal enhancement that has proven useful in the study of single lipid bilayer systems is to deposit a Au layer, about 100 Å thick, onto a Si substrate. Then the film of interest is affixed to the gold layer: *e.g.*, an alkane thiol layer followed by a phospholipid layer, and then a backing with a D₂O reservoir [40]. Because the reflectivity can be calculated for a model of such a system, it is relatively easy to determine a feasible combination of the film of interest and signal boosting layers, or surrounding media, that significantly increase the sensitivity of the measurement.

3.15 Multilayer Samples: Secondary Extinction and Mosaic

In discussing the theoretical treatment of multilayer reflectivity within the Born approximation, it is implicit that the reflectivity is sufficiently low that

the reflectivity of a given reflection order is proportional to the square of the number of bilayers M , as we derived above. However, in practice, multilayer samples of lipid bilayers actually form structures similar to mosaic crystals, having an angular distribution of coherently scattering blocks, each consisting of a stack of bilayers. This angular distribution typically is centered about the mean surface normal of the substrate, with the normal of an individual block perpendicular to the plane of the lipid bilayers in that stack. As the incident beam penetrates such a sample, its intensity can be diminished by successive reflections from various stacks, so that a given reflection peak intensity no longer is proportional to M^2 . This troublesome effect, called secondary extinction [5, 29, 41, 42], introduces further complications into the multilayer analysis. It is necessary to recognize and take into account secondary extinction when it occurs so that an error is not made in determining relative reflection peak intensities. Recently, multibilayers of biofilm materials have been made with a well-defined, relatively small number of bilayer repeats which are appropriate for analysis using the dynamical theory outlined in Section 2.1 [43].

3.16 Data Collection Strategies for Time-Dependent Phenomena

In measuring specular reflectivity from thin film systems which may undergo structural changes with time, specular scans must be performed over a given range of Q in a time less than that required for any significant changes to occur. This can be directly determined by superimposing reflectivity plots for successive scans; successive runs can be added together to improve statistical accuracy once equilibrium has been achieved. Whether the film under study exhibits time-dependent behavior or not, it is prudent to perform rocking curves in between specular or other scans, such as background, to verify correct alignment of the sample.

4 Phase Determination Techniques

Earlier in the chapter we discussed the connection between the phase of the complex reflection amplitude and the uniqueness of SLD profiles. Here we continue discussion of phase-sensitive specular reflectometry techniques, outlining practical methods for determining the phase of reflection for a film of interest using reflectivity measurements of composite film structures, *i.e.*, film sandwiches composed of the "unknown" film adjacent to a reference layer or to a known surrounding medium. These methods have been recently reviewed in depth [11].

4.1 Reference Films

Figure 16a illustrates the measurements which are performed to determine the SLD profile of a film, in this case a Cr/Au layer deposited on a Si substrate.

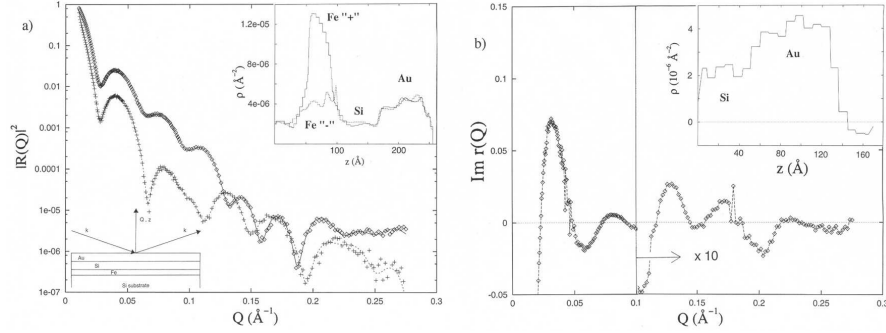


Fig. 16. Diagram illustrating the measurements which are performed to determine the SLD profile of an "unknown" film, in this case a Cr/Au layer deposited on a Si substrate which functions as the incident or fronting medium as well (a). By measuring two reflectivity data sets the imaginary part of the reflection amplitude for the "unknown" film of interest, in this example the Cr/Au layers, can be determined uniquely at each value of Q ; the result is shown in (b). The upper right corner inset of (a) shows the SLD profiles corresponding to independent fits of the reflectivities for the two composite film systems. The imaginary part of the reflection amplitude can then be inverted by a first principles calculation, as discussed in the text, the result of which is also shown in (b). (After Figs. 2 and 3 of ref. [48].)

The reference layer consists of a ferromagnetic Fe layer with a magnetization which is saturated in the plane of the film. For a polarized neutron in the "+" spin state (one of two possible spin eigenstates), the SLD of the Fe layer is a sum of two parts, one associated with the nuclear interaction and the other with the magnetic potential which exists between the magnetic moments of the neutron and the Fe atoms. In contrast, a neutron polarized in the "-" state sees a SLD which is the difference of the nuclear and magnetic components. By measuring two reflectivity data sets, one with a beam of neutrons in the "+" spin state and the other in the "-" state, plotted in Fig. 16a, the imaginary part of the reflection amplitude for the the Cr/Au film, can be determined uniquely, exactly and independently at each Q [48]. The result is shown in Fig. 16b. The imaginary part of the reflection amplitude can then be inverted by a first principles calculation [26, 46, 47]. (More formally, either $\text{Re } r(Q)$ or $\text{Im } r(Q)$ suffices for most of the SLD profiles of interest to biology.) The result of inverting $\text{Im } r(Q)$ of Fig. 16b is also shown in the figure. The SLD profile so obtained is unique, to the extent allowed by the finite wavevector range over which the original reflectivity data was collected. In solving for $\text{Im } r(Q)$ of the unknown, two roots of a quadratic equation are obtained, only one of which is physical [25, 48]. The physical branch $\text{Im } r(Q)$ can be determined, in principle, because $\text{Im } r(Q)$ must be a continuous function of Q with known behavior at the origin, *viz.*, $\text{Im } r(Q) \leftarrow 0$ from negative values for an overall positive SLD. However, it can happen in practice that the separation of the two

branches is problematic, especially for noisy data. The use of three reference layers eliminates this problem—and, in fact, was the first of the exact reference techniques for specular reflection [22, 23, 49]—but three references are difficult to achieve using a single magnetic layer. Furthermore, in any finite reference layer method for phase determination, the entire SLD density profile of each reference layer used must be known with an accuracy commensurate with the spatial resolution desired in the sample film profile. And of course, magnetic references, in particular, require the availability of polarized neutron beams.

4.2 Surround Variation

A reference method closely related to that employing different layers of finite thickness, as described above, involves varying the surrounding media, fronting or backing. This "variation on a theme" has the important advantage that only two constant SLD values, for either the fronting or backing, are required to obtain $\text{Re}r(Q)$ corresponding to the sample film, independently at each Q , and without branch ambiguities [24], since, the resulting surround variation equations are linear. One approach that has been successfully employed involves depositing the sample film on two different substrates, *e.g.*, Al_2O_3 and Si, simultaneously and under identical conditions [27]. Care must be taken to limit any differences between the two samples which could be present, such as the presence of a native oxide layer on the Si or a layer of different SLD on the Al_2O_3 due to the effects of surface polishing.

A less cumbersome approach employs a single sample and an adjacent liquid reservoir of variable SLD. Figure 17a contains a schematic of a surround variation method for phase determination in which the backing medium SLD can have (at least) two values, in this particular example that of D_2O and Si—(SLD) matched water—*i.e.*, an H_2O and D_2O mixture with approximately 38 % D_2O by volume. Figure 17 also shows the corresponding composite reflectivity curves for these two backing media adjacent to the Cr/Fe/Au/alkane thiol film indicated in the upper right hand corner of the figure. This is similar to the film structure of Fig. 16, except that the Fe "+" and "-" layers are now treated as part of the "unknown" film. Included in Fig. 17a is $\text{Re}r(Q)$ for the unknown film, one in which the SLD of the saturated magnetization of the ferromagnetic Fe layer is that seen by a spin "+" state neutron beam. Lastly, Fig. 17b shows the SLD profile obtained by direct inversion of the $\text{Re}r(Q)$ of Fig. 17a. For comparison, the SLD profile obtained for the "-" state neutron beam is also shown [45]. Note the consistency of the two results; the Au layer SLD is virtually identical in both sandwich structures, the one with the Fe "+" layer and the other with the Fe "-" film.

4.3 A "Sweet Solution"

Given the importance and ubiquity of aqueous solutions in the study of biomembranes, the method of choice in phase-sensitive reflectivity measurements would very likely be variation of the backing medium using a suitable

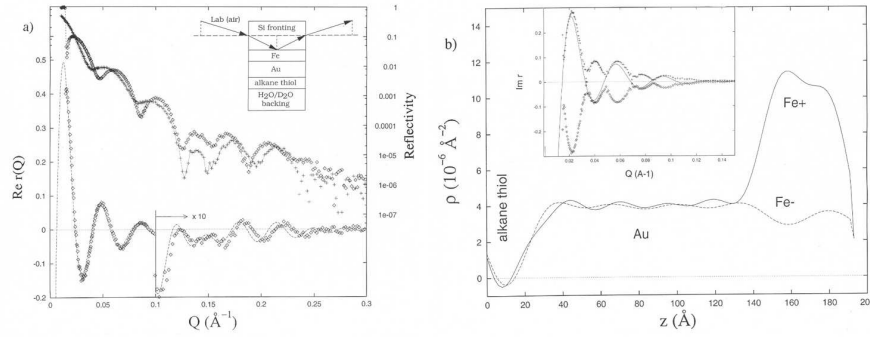


Fig. 17. Schematic representation of a surround variation method for phase determination in which the backing medium SLD can have (at least) two values, in this particular example that of D_2O and Si-SLD-matched water (a). (a) plots the corresponding composite reflectivity curves for these two backing media SLD values adjacent to the Cr/Fe+/Au/alkane-thiol film; note that this is similar to the film structure of Fig. 16 except that the Fe "+" layer is now treated as part of the "unknown" film. (a) also shows $Re r(Q)$ for the "unknown" film, one in which the SLD of the saturated magnetization of the ferromagnetic Fe layer is that seen by a spin "+" state neutron beam. Lastly, (b) shows the SLD profile obtained by direct inversion of $Re r(Q)$ of (a). For comparison, the SLD profile obtained for the "-" state neutron beam is also shown. (After Figs. 1 and 2 of ref. [45].)

fluid, except for one crucial concern. If the fluid differentially penetrates the adjacent film of interest, then the reference measurement is destined to fail, since an essential premise of the technique is that the film of interest be invariant to the change in references. This restriction therefore precludes the use of variation by D_2O/H_2O substitution if water penetrates the membrane, which indeed is known to occur. This problem can be solved if an aqueous solution could be found in which a suitable solute is the agent of SLD variation without interfering with the film: possibly, for example, a sugar in D_2O , where sugar molecules—of variable concentration—do not penetrate or modify the film, whether or not the constant D_2O component is integral to the film. This would indeed be a "sweet solution" for surround variation in some problems.

4.4 Refinement

The formal inversion methods alluded to earlier begin with a Fourier transform of $Re r(Q)$ and thus require this information at all values of Q for exact implementation. Thus, the resulting SLD profiles are distorted by unavoidable data truncation, the effect decreasing systematically with increasing Q_{max} . This means that the $\rho(z|Q_{max})$ obtained by inverting $Re r(Q|Q_{max})$ will not exactly reproduce $Re r(Q|Q_{max})$ without additional refinement. Useful approaches to this problem [51, 18, 12] take $\rho(z|Q_{max})$ as a starting point for

model independent fitting procedures designed to accept only spatial detail consistent with the spatial resolution, $l = \pi/Q_{\max}$. The resulting refinement, say, $\tilde{\rho}(z|Q_{\max})$, effectively represents the most that can be said about the veridical $\rho(z)$ at the given resolution.

4.5 Diagnostics

Only the real part of the reflection amplitude, $\text{Re } r(Q)$, is necessary to obtain the SLD profile by first-principles inversion for most films of interest, as mentioned in our discussion of surround variation, Sec. 4.2. Now the same information which gives $\text{Re } r(Q)$ also predicts $\text{Im } r(Q)$, but only up to a quadratic branch ambiguity, similar to that discussed in Sec. 4.1 for the technique using two finite references layers. This ambiguity is of no concern to obtaining $\rho(z)$, but the ancillary, if incomplete, knowledge of $\text{Im } r(Q)$ that also results from surround variation happens to a useful diagnostic of film quality, because of a seemingly arcane mathematical property of $r(Q)$. It turns out that for a perfect but arbitrary film of thickness L , the spectrum of $\text{Im } r(Q)$ must possess a more-or-less uniform sequence of zeroes near multiples of $Q = 2\pi/L$, suggestive of the Kiessig fringes seen in the reflectivity, as described in Sec. 3.3 [45]. On the other hand, $\text{Re } r(Q)$ need display these zeros only if the film is perfectly centrosymmetric. So, in fact, the Kiessig fringes observed in $|r(Q)|^2$ normally are not the manifestation of zeros in $r(Q)$ but rather of $\text{Im } r(Q)$ alone. In physical terms, these zeros are a property of coherent reflection from laterally homogeneous film and are readily detectable even in the presence of branch ambiguities. The absence of zeros, *i.e.*, the presence of branch "splittings" in $\text{Im } r(Q)$, thus is a strong indication that the film under study is defective in these terms.

For example, as discussed in Sec. 3.3, if a film is laterally inhomogeneous on a scale large compared to the neutron coherence length, then the measured specular reflectivity is an average of areally weighted reflectivities from the separate inhomogeneous components, as given in eq. 20. In this case, there is no single SLD profile associated with the measured reflectivity, and any attempt to extract one, whether by inversion or fitting techniques, will produce unphysical results. The absence of $\text{Im } r(Q)$ splittings, beyond those consistent with noise effects, are a good indication of acceptable film quality [27]. (A film much thicker than the neutron coherence length can also cause a loss of $\text{Im } r(Q)$ zeros, in line with the discussion in Sec. 3.3; but this can be tested instrumentally and normally is not a concern for thin films.)

5 An Illustrative Example

To illustrate the application of neutron reflectometry to the study of biofilms, we consider the recent structural investigation of a hybrid bilayer membrane

(HBM) and its interaction with melittin [40]. In this particular study, specular neutron reflectometry was used to probe the interactions of the peptide toxin, melittin, with supported bilayers of phospholipid (d54-dimyristoyl phosphatidylcholine or dDMPC) and octadecanethiol ($\text{HS}(\text{CH}_2)_{17}\text{CH}_3$) or thiahexa(ethylene oxide) alkane ($\text{HS}(\text{C}_2\text{H}_4\text{O})_6(\text{CH}_2)_{17}\text{CH}_3$ or THEO-C18) on gold. This supported lipid bilayer consisting of adjacent "leaflets" of alkanethiol and phospholipid forms a model biomimetic membrane. The primary objectives of the study were to locate the position and orientation of the melittin within the membrane and also to determine whether the ethylene oxide moieties are hydrated when the HBM is in contact with water. Sample preparation and other details of the experiments and analysis can be found in the original work [40]. Figure 18 shows the SLD profiles of the THEO-C18/dDMPC HBMs next to a D_2O reservoir with and without melittin, as obtained from model-independent fitting of the corresponding reflectivity data plotted in the inset [40]. Note that $Q_{\text{max}} \approx 0.73 \text{ \AA}^{-1}$, corresponding to a spatial resolution about 0.5 nm.

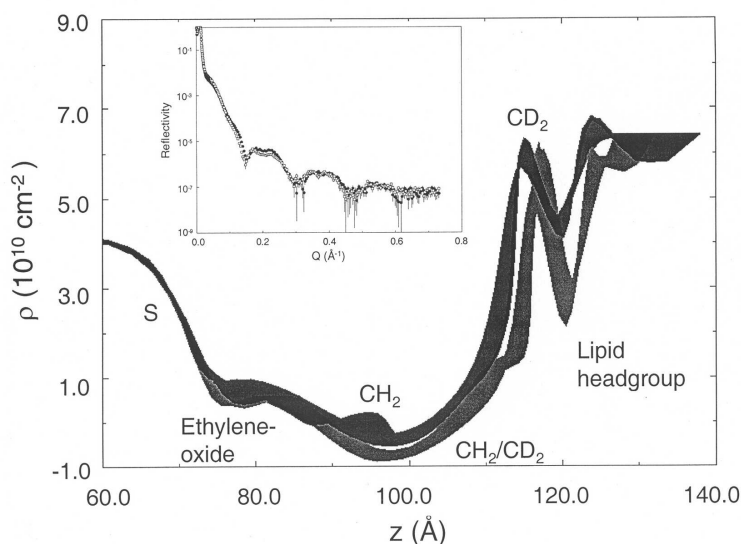


Fig. 18. SLD profiles of the THEO-C18/dDMPC HBMs described in the text next to a D_2O reservoir with and without melittin (darker shaded thick curve) as obtained from model-independent fitting of the corresponding reflectivity data (filled symbols without melittin) plotted in the inset [40]. (The Cr/Au metal layers, Cr, 20 Å thick, and Au, 65 Å thick, on Si, are not shown.) Note that $Q_{\text{max}} \approx 0.73 \text{ \AA}^{-1}$, corresponding to a spatial resolution about 0.5 nm.

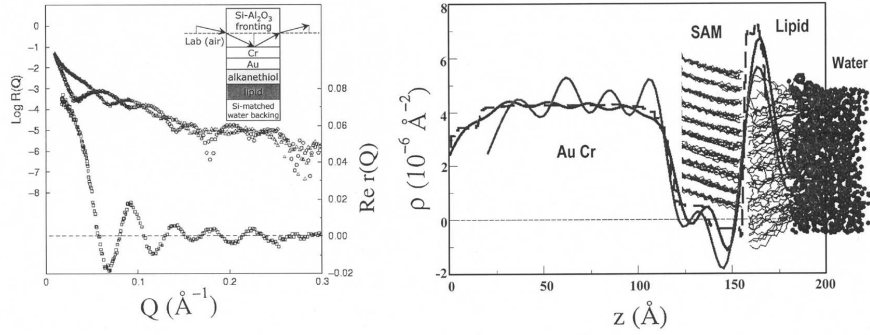


Fig. 19. Phase-sensitive neutron reflectivity measurements performed on a self-assembled THEO-C18 layer on a Cr/Au metallic bilayer, pre-deposited on Si and Al₂O₃ single crystal substrates, followed by a dDMPC layer (left). $\text{Re } r(Q)$ for the common film sandwich determined from that reflectivity data is shown in the lower part, along with a schematic for the phase-sensitive reflectivity measurements in the upper right corner (details of the neutron reflectivity measurements and analysis are given in [27]). SLD profile obtained by first-principles inversion (solid curve with the more pronounced oscillations in the Au/Cr region due in part to truncation of the data at Q_{max}) of the $\text{Re } r(Q)$ (right) [27]. This unique solution is compared to the prediction of a molecular dynamics simulation (other solid curve) [31].

In order to verify that profiles so obtained were physically meaningful, phase-sensitive neutron reflectivity measurements were performed [27] on an almost identical pair of samples: self-assembled THEO-C18 on a Cr/Au metallic bilayer, predeposited on Si and Al₂O₃ single crystal substrates, followed by the dDMPC layer. In this case, the Si and Al₂O₃ substrates served as two different fronting media, with a common backing of Si SLD-matched water, for collection of the pair of composite reflectivity data sets shown in Fig. 19. $\text{Re } r(Q)$ for the common film sandwich determined from that reflectivity data by the surround variation solution is also shown in the figure, along with a schematic for the phase-sensitive reflectivity measurements [27]. Figure 19 shows the $\rho(z)$ obtained by first-principles inversion of the $\text{Re } r(Q)$ using the techniques of Sec. 4.2. This unique solution is compared to the prediction of a molecular dynamics simulation [31]. The close similarity of the SLD profiles of Fig. 18 (without melittin) and Fig. 19, gives confidence in the results.

The neutron reflectivity study described above indicates that melittin strongly perturbs the phospholipid headgroup region, but also affects the alkane chain region of the bilayer. Among other findings [40], these results demonstrate the utility of neutron reflectometry in determining subnanometer structural changes in biomimetic membranes caused by biologically relevant molecules.

References

1. B. Alberts, D. Bray, J. Lewis, M. Raff, K. Roberts and J. D. Watson, *The Cell*, 3rd Ed., (Garland Publishing, New York, 1994). Roberts and J. D. Watson, *The Cell*, 3rd Ed., (Garland Publishing, New York, 1994).
2. S. K. Sinha, E. B. Sirota, S. Garoff and H. B. Stanley, *Phys. Rev. B* 38, 2297 (1988).
3. R. Pynn, *Phys. Rev. B* 45, 602 (1992).
4. S. Krueger, *Current Opinion in Colloid & Interface Science* 6, 111 (2001).
5. G. E. Bacon, *Neutron Diffraction*, 3rd Ed., (Oxford University Press, London, 1975).
6. J. Penfold and R. K. Thomas, *J. Phys.: Condens. Matter* 2, 1369 (1990).
7. T. P. Russell, *Matls. Sci. Reps.* 5, 171 (1990).
8. *X-ray and Neutron Reflectivity: Principles and Applications*, J. Daillant and A. Gibaud, Eds., (Springer, Berlin, 1999).
9. C. F. Majkrzak, *Acta Physica Polonica A* 96, 81 (1999).
10. C. F. Majkrzak, J. Kwo, M. Hong, Y. Yafet, D. Gibbs, C. L. Chien and J. Bohr, *Advances in Physics* 40, 99 (1991).
11. C. F. Majkrzak, N. F. Berk and U. Perez-Salas, *Langmuir* 19, 7796 (2003).
12. N. F. Berk and C. F. Majkrzak, *Langmuir* 19, 7811 (2003).
13. E. Merzbacher, *Quantum Mechanics*, 2nd Ed., (Wiley, New York, 1970).
14. N. F. Berk and C. F. Majkrzak, unpublished.
15. M. Born and E. Wolf, *Principles of Optics*, (Pergammon Press, Oxford, 1987) p.51.
16. C. F. Majkrzak and N. F. Berk, *Physica B* 336, 27 (2003).
17. J. F. Ankner and C. F. Majkrzak, in *SPIE Proc.* 1738, C. F. Majkrzak and J. L. Wood, Eds. (SPIE, Bellingham, WA, 1992) 260.
18. N. F. Berk and C. F. Majkrzak, *Phys. Rev. B* 51 (1995) 11296.
19. G. Fragneto, R. K. Thomas, A. R. Rennie, and J. Penfold, *Science* 267, 657 (1995).
20. W. Leslauer and J.K. Blasie, *Acta Cryst. A* 27 (1971) 456.
21. M. K. Sanyal, S. K. Sinha, A. Gibaud, K. G. Huang, B. L. Carvalho, M. Rafailovich, J. Sokolov, X. Zhao, W. Zhao, *Europhysics Lett.* 21 (1993) 691.
22. C. F. Majkrzak, N. F. Berk, *Phys. Rev. B* 1995, 52, 10827.
23. V. O. de Haan, A. A. van Well, S. Adenwalla, G. P. Felcher, *Phys. Rev. B* 1995, 52, 10831.
24. C. F. Majkrzak, N. F. Berk, *Phys. Rev. B* 1998, 58, 15416. (Erratum *Phys. Rev. B* 60, 16211.)
25. R. Lipperheide, J. Kasper, H. Leeb, *Physica B* 1998, 248, 366.
26. K. Chadani and P. C. Sabattier, *Inverse Problems in Quantum Scattering Theory* (Springer, New York, 1989).
27. C. F. Majkrzak, N. F. Berk, S. Krueger, J. A. Dura, M. Tarek, D. Tobias, V. Silin, C. W. Meuse, J. Woodward, A. L. Plant, *Biophysical Journal* 79, 3330 (2000).
28. C. F. Majkrzak, N. F. Berk, Doon Gibbs, in *Magnetic Multilayers*, Edited by L. E. Bennett and R. E. Watson, (World Scientific, Singapore, 1994) p. 299.
29. M. C. Wiener and S. H. White, *Biophys. J.* 59, 162 (1991).
30. J. K. Blasie, B. P. Schoenborn and G. Zaccai, in *Neutron Scattering for the Analysis of Biological Structures*, Brookhaven Symposia in Biology No. 27 (BNL50453) (NTIS, Springfield, VA, 1976) p. III-58.

31. M. Tarek, K. Tu, M. L. Klein and D. J. Tobias, *Biophys. J.* 77, 964 (1999).
32. C. F. Majkrzak, *Physica B* 221, 342 (1996).
33. R. Gahler, J. Felber, F. Mezei and R. Golub, *Phys. Rev. A* 58, 280 (1998).
34. S. K. Sinha, M. Tolan and A. Gibaud, *Phys. Rev. B* 57, 2740 (1998).
35. H. J. Bernstein and F. E. Low, *Phys. Rev. Letts.* 59, 951 (1987).
36. R. Golub and S. K. Lamoreaux, *Physics Letters A* 162, 122 (1992).
37. H. Rauch and S. A. Werner, *Neutron Interferometry*, (Clarendon Press, Oxford, 2000).
38. A. Zeilinger, R. Gahler, C. G. Shull and W. Treimer, *AIP Conf. Proc. Neutron Scattering*, Ed. J. Faber, (AIP, 1982) p.93.
39. A. Steyerl, K. A. Steinhauser, S. S. Malik, and N. Achiwa, *J. Phys. D, Appl. Phys.* 18, 9 (1985).
40. S. Krueger, C. W. Meuse, C. F. Majkrzak, J. A. Dura, N. F. Berk, M. Tarek, A. L. Plant, *Langmuir* 17, 511 (2001).
41. M. J. Yeager, in *Neutron Scattering for the Analysis of Biological Structures*, Brookhaven Symposia in Biology No. 27 (BNL50453) (NTIS, Springfield, VA, 1976) p. VII-77.
42. D. L. Worcester, in *Neutron Scattering for the Analysis of Biological Structures*, Brookhaven Symposia in Biology No. 27 (BNL50453) (NTIS, Springfield, VA, 1976) p. III-37.
43. U. Mennicke and T. Salditt, *Langmuir* 18, 8172 (2002).
44. K.-M. Zimmermann, M. Tolan, R. Weber, J. Stettner, A. K. Doerr, W. Press, *Phys. Rev. B* 62, 10377 (2000).
45. C. F. Majkrzak, N. F. Berk, V. Silin and C. W. Meuse, *Physica B* 283, 248 (2000).
46. P. E. Sacks, *Wave Motion* 18, 21 (1993).
47. N. F. Berk, C. F. Majkrzak, *J. Phys. Soc. Jpn.* 65, Suppl. A, 107 (1996).
48. C. F. Majkrzak and N. F. Berk, *Physica B* 267-268, 168 (1999).
49. C. F. Majkrzak, N. F. Berk, J. A. Dura, S. K. Satija, A. Karim, J. Pedulla and R. D. Deslattes, *Physica B* 248, 338 (1998).
50. J. M. Cowley, *Diffraction Physics*, (North Holland, Amsterdam, 1990) p.131.
51. C. F. Majkrzak and N. F. Berk, *Appl. Phys. A* 74, S67 (2002).
52. R. G. Nuzzo, F. A. Fusco, D. L. Allara, *J. Am. Chem. Soc.* 109, 2358 (1987).